

AN ASSESSMENT OF SENTINEL-1 RADAR IMAGERY TIME-SERIES ANALYSIS FOR MONITORING SEASONAL SURFACE SUBSIDENCE DUE TO PERMAFROST DEGRADATION AFTER A TUNDRA FIRE

Gijs van Leeuwen - 2597103

12-7-2019

Abstract

The permafrost areas in high latitude regions hold two atmospheres worth of carbon and are prone to climate warming. Fire is a major disturbance in these regions as shown by the 2017 Greenland fire (17,3 km²) which is investigated in this research. With new advancements as persistent scatterer interferometry time-series analysis and improvements in revisit time of new satellite constellations, it has become possible to compute surface displacements with mm accuracy over natural areas. Using Stanford method for persistent scatterers and Sentinel-1 data of the pre- and post-fire year the mean seasonal vertical displacement velocities have been computed for the area of and around the fire scar. The mean relative displacement velocity within the fire scar is -10.75 mm/y for 2016 and -2.90 mm/y for 2018 and outside the fire scar is -15.79 mm/y for 2016 and -4.95 mm/y for 2018. The normalized difference of the burned and unburned area from 2016 to 2018 is -4.00 mm/y of impact on the burned area. The mean standard deviation over the area of interest is 10,65 and 8,85 mm/year respectively for 2016 and 2018. The DNBR fire severity, retrieved from Sentinel-2 imagery, had a significant but minor relation with the mean displacement velocities of -2.02 mm/yr. The minor trend may be due to the thin tundra soils in the study area which, therefore contains little organic matter for combustion hence the fire impact on the organic soil was relatively minor. The study confirms the utility of Persistent Scatterer Interferometric Synthetic Aperture Radar (PS-InSAR) for seasonal surface subsidence in tundra environments. With additional years of data coming, further research could focus on fire impacts in tundra regions with thicker soils and possibly account for interannual weather variability in the thaw season using improved methods.

Keywords: PS-InSAR, permafrost, tundra fire, subsidence, Sentinel-1, StAMPS

*Supervision by dr. Sander Veraverbeke and dr. Kanayim Teshebaeva
part of course AB_1096, Bachelor thesis earth sciences.*

For the Vrije Universiteit (VU) Amsterdam faculty for beta sciences cluster earth and climate

Table of contents

1. INTRODUCTION	2
2. METHODS	4
2.1 Data.....	4
2.1.1 Sentinel-1	4
2.1.2 Sentinel-2	5
2.1.3 DEM	5
2.2 PS-InSAR processing.....	6
2.2.1 Background on DInSAR for computing displacement	6
2.2.2 Pre-processing using SNAP	8
2.2.3 Processing using StaMPS	9
2.3 Analysis of environmental drivers of subsidence	10
3. RESULTS	12
3.1 PS-InSAR	13
3.2 Environmental drivers.....	15
3.2.1 Displacement in relation to fire severity and greenness	15
3.2.2 Displacement in relation to relief	19
4. DISCUSSION	20
4.1 PS-InSAR complications and possibilities.....	20
4.2 Effect of tundra fire on subsurface displacements	21
4.3 Relation of displacement with greenness and topography	21
4.4 Recommendations for future research	21
5. CONCLUSIONS	22
6. ACKNOWLEDGEMENTS	22
7. REFERENCES	23
8. APPENDICES	27

1. INTRODUCTION

Fire is a major disturbance in local tundra dynamics [Rocha et al., 2012], with large impacts on permafrost [Gibson et al. 2018], the carbon cycle [Bowman et al., 2009] and soil characteristics. Especially the long-term impact on the seasonal thaw cycle [Rocha and shaver, 2011], caused by increasing active layer thickness is an important forcing. A decrease in albedo of the burned surface area and decrease in thickness of the insulating layer are both fire-induced positive feedbacks on permafrost degradation [Mazhitova, 2000]. The darker burned area absorbs more solar radiation contributing to a thicker active layer [Hinzman et al., 1991]. Fire consumes a part of the top organic soil, which acts as an insulating layer. By doing so permafrost may be more vulnerable to thawing resulting in a thicker active layer. Fires in arctic regions trigger thermokarst, leaving gigantic impact on local soil and hydrological conditions [Rocha et al., 2012]; contributing to CO₂ and CH₄ emissions [Schuur et al., 2008] and can lead to permafrost collapse leading to significant changes in surface hydrology [Zoltai 1993]. Other climate forcings include the decrease of the Greenland ice sheet albedo, caused by soot that is deposited on the ice sheet [Hansen and Nazarenko, 2004], and direct carbon emissions from peat burning. Permafrost regions are changing rapidly due to climate warning [Lawrence et al., 2008] and more frequent extreme weather [Flannigan et al., 2008]. Peatland fires have long-term effects on the ecosystem for several decades by deepening and warming the active layer and spatial expansion of continuously thawed soil layers (taliks) [Gibson et al., 2018].

Both direct thaw of local ice and the thickening of the active layer result in surface subsidence [Liu et al., 2014]. Firstly, the freezing soil water and thawing ground ice in seasonally exposed tundra trigger frost heave in winter, and therefore subsidence in summer; resulting from the higher water content in a thicker active layer is an increased ground subsidence as these have direct relation [Liu et al., 2012]. Fire-induced thaw of ice-rich permafrost may melt ground ice, this process can be expected to be local and irregular in some situations. The continuity of this subsidence is dependent on local thaw dynamics: either top-down thawing of the permafrost leaves a continuous subsidence or local irregular ice thawing results in thermokarst landscape artefacts [Iwahana et al., 2016].

Subsidence can be monitored from space using Synthetic Aperture Radar (SAR) acquisitions to compute phase differences between two acquisitions which, can be translated into displacement. The sentinel-1 constellation provides active SAR imagery with satellite Sentinel-1A since 2015 and with the recent addition of the Sentinel-1B satellite the Area Of Interest (AOI) is revisited every 6 days. This improved revisit time opens possibilities for time-series analysis over shorter time periods and therefore, seasonal subsidence calculation. Using recent methods, the relative vertical displacements are calculated with mm precision [Delgado Blasco et al., 2019; Foroughnia et al., 2019; Gunce et al., 2017; Hooper et al., 2007; Liu et al., 2014 and Prats-Iraola et al., 2016].

The AOI for this case study is located on the west coast of Greenland (figure 1.1) and in 2017 a tundra fire left the area a record-breaking fire scar (Figure 1.2). Although some small fires occur in Greenland annually, the extent of this fire was unseen in at least the satellite record and shook scientists and media. The fire was active from July 31 to August 21, 2017 and left 17,3 km² of burned area 150 kms north-east of the 2nd largest city in Greenland, Sisimut. The area has a mean slope and mean height of 208m and 9.4 degrees respectively [Howat, Negrete, Smith, 2015], with vegetation characterized as erect dwarf-shrub tundra and low-shrub tundra [CAVM Team.

2003]. The area is at 68 degrees latitude resulting in a mean annual temperature of around -10 degrees Celsius [Dee et al, 2011]. Because of the low temperature this area falls within the permafrost region, ground (soil, sediment, or rock) that remains at or below 0°C for at least two years [Permafrost Subcommittee, 1988]. The permafrost in this study area is classified as a continuous permafrost with low ground ice content, thin overburden and exposed bedrock [Brown et al., 2002].

Based on Radio Detection And Ranging (radar) data of the study area, during the Greenland thawing season of 2016 and 2018, seasonal subsidence before and after the fire was computed. I used seasonal surface displacement from radar imagery to examine the impacts of tundra fires on short-term seasonal permafrost degradation [Liu et al., 2014, Iwahana et al., 2016]. Furthermore, I studied spatial patterns of seasonal subsidence in relation to environmental variables including fire severity, vegetation cover and topography and determined the utility of Persistent Scatterer Interferometric Synthetic Aperture Radar (PS-InSAR) with Sentinel-1 imagery for seasonal subsidence research.

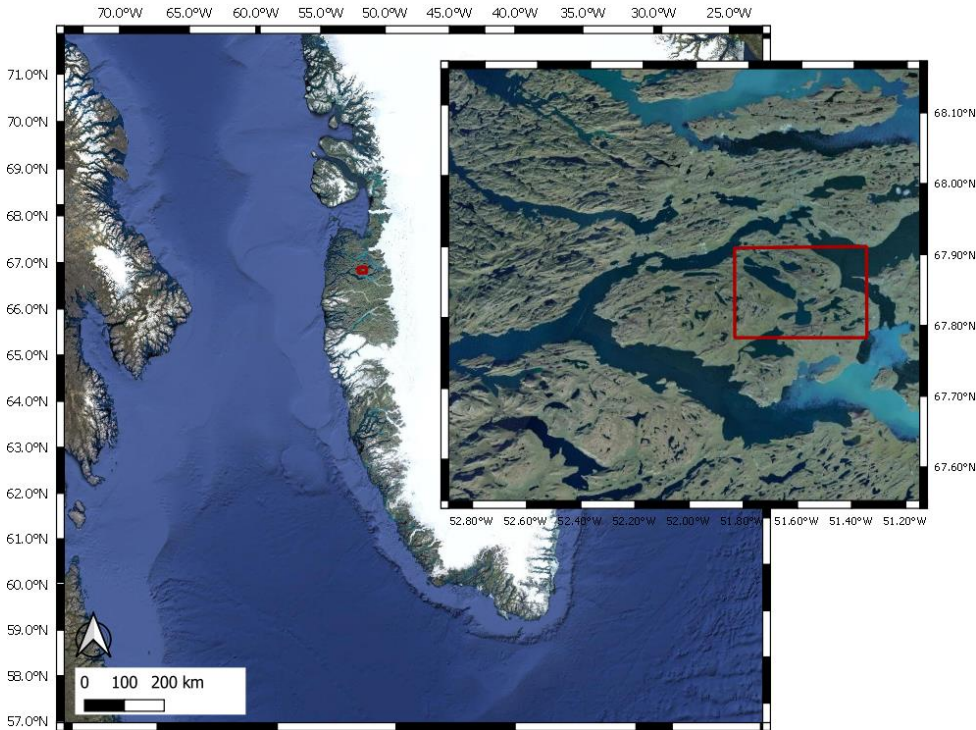


Figure 1.1 The study area on the West coast of Greenland represented with a red rectangle on Google Earth satellite imagery

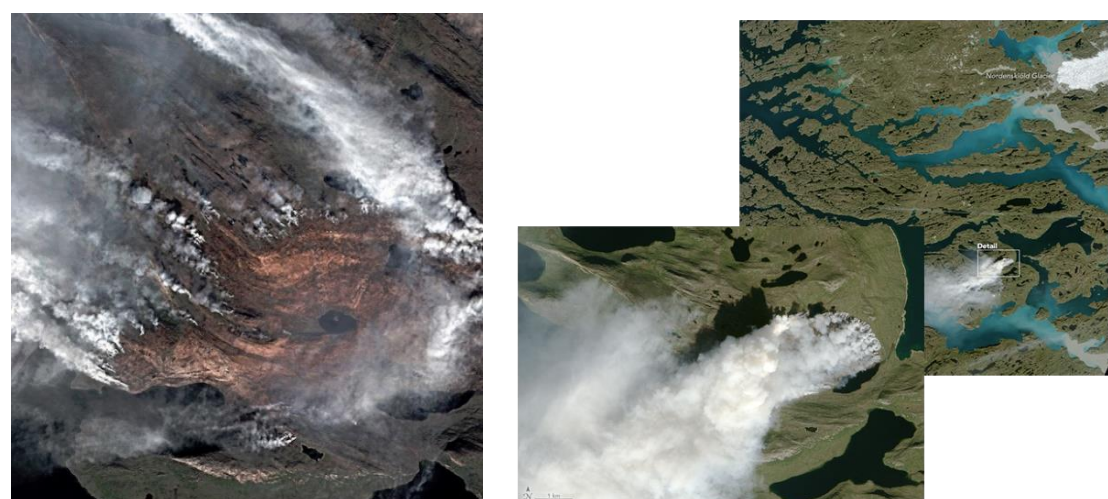


Figure 1.1 Deimos imagery from august 8 2017 and Landsat imagery from august 3 showing the impact of the fire. images from NASA earth Observatory news post.

2. METHODS

Subsidence of the study area is calculated using SAR imagery in European Space Agency's (ESA) Sentinel Application Platform (SNAP) S1-toolbox [Veci et al., 2014] and Stanford Method for Persistent Scatterers (StaMPS) by the University of Leeds [Hooper, 2008, Hooper et al., 2007; Hooper et al., 2012]. This Interferometric Synthetic Aperture Radar (InSAR) processing chain was based on multiple open source toolboxes by using Copernicus Sentinel-1 satellite data. The interferometric pre-processing of the radar data was performed using the Python wrapper package Snap2StaMPS [Foumelis et al., 2018]. Combining the single master interferometry pre-processing from SNAP and the spatial correlation Persistent Scatterer (PS) algorithm [Hooper et al., 2004] from StaMPS the Line Of Sight (LOS) displacements are retrieved. StaMPS uses the Statistical-cost, Network-flow Algorithm for Phase Unwrapping (SNAPHU) [Chen and Zebker, 2001] for the unwrapping of the interferometric phase and implements the Toolbox for Reducing Atmospheric InSAR Noise (TRAIN) [Bekeart et al., 2015]. The processing chain is dependent on the Greenland Ice Mapping Project (GIMP) Digital Elevation Model (DEM) [Howat, Negrete, Smith, 2014] for the topographic processing parts. Sentinel-2 data from 2017 is used to perform an analysis of the displacement with multiple environment variables.

2.1 Data

The Copernicus Sentinel program by the European Space Agency (ESA) supplies open source data complete transparency in real time [retrieved from Alaska Satellite Facility (ASF), processed by ESA – 2019]. Both Sentinel-1 and Sentinel-2 data are used in this case study to compute the displacement and evaluate relationships between the displacement and environmental variables.

2.1.1 Sentinel-1

The Sentinel-1 constellation consists of 2 satellites, Sentinel-1A and Sentinel-1B, that have been operating since October 2014 and April 2016. The satellites supply 250km Interferometric Wide (IW) swath images in C-band through all-weather conditions with 10m ground resolution, all images acquired are shown in table 1. The images are available in the level 1-SLC format that consists of the phase and amplitude information measured by the active SAR sensor. Images are available in multiple polarizations but for this case study only the dual polarization option HH is used as it is proven to be best for DInSAR [Ittycheria, Vaka and Rao, 2018]. Sentinel-1 is used because C-band has good displacement accuracy in comparison to L- or X-band SAR and the increased temporal decorrelation of C-band is remedied with the use of PS-processing [Pepe and Caló, 2017]. Sentinel-1 has frequent

Satellite	Date of Acquisition	Orbit pass	Path/frame	Polarization/incidence angle	Subswath/bursts	N_Aquisitions	Master date
SIA	2016/06/20-2016/09/30	Ascending	90/~222	HH/32.9	IW1/1-3	10	2016/08/01
SIA	2016/05/29-2016/09/26	Descending	25/~365	HH/38.3	IW2/6-8	10	2016/07/16
SIA	2016/06/05-2016/10/03	Descending	127/~366	HH/43.1	IW3/5-7	10	2016/07/23
SIA /SIB	2018/06/10-2018/09/26	Ascending	90/~222	HH/32.9	IW1/1-3	19	2018/08/03
SIA /SIB	2018/05/31-2018/10/04	Descending	25/~365	HH/38.3	IW2/6-8	20	2018/07/30
SIA /SIB	2018/06/01-2018/09/29	Descending	127/~366	HH/43.1	IW3/5-7	20	2018/07/25

Table 1 Data overview of all Sentinel-1 acquisitions used for displacement computation including the incidence angle and master dates.

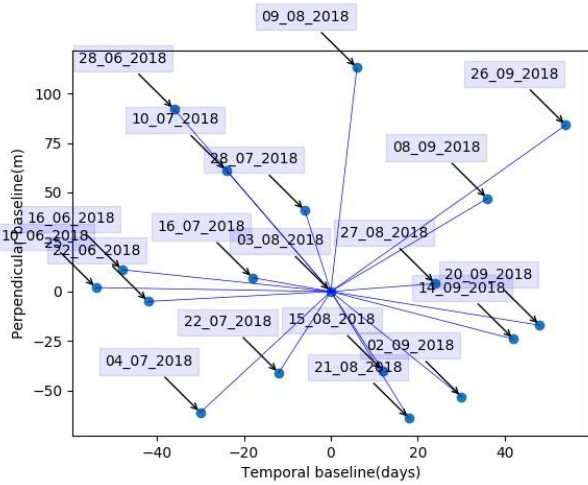


Figure 2.1.1.2 Plot of the baseline and temporal differences between slaves and single master image for descending track 25/-365, year 2018

imagery over this area of Greenland since it is a focus area for cryospheric studies of the Greenland ice sheet. With a revisit time of 6 days, when combining

Sentinel-1A and Sentinel-1B, the Sentinel-1 mission is a large improvement on the older ESA radar missions European Remote Sensing (ERS) and Environmental Satellite (Envisat) that had a 35-day repeat cycle. The specific image acquisition used is Terrain Observation by Progressive Scans (TOPS) [De Zan and Guarnieri, 2006] that can be handled using the SNAP S1-toolbox. The images for this case study are from ascending track 90/-222 and descending tracks 25/-365 And 127/-366 (Figure 2.1.1.1). The processing is separate for each year since we are interested in the seasonal deformation. The processing is also separate for each track since ascending and descending images cannot be combined in InSAR processing due to orbital differences. The perpendicular baseline information in relation to the temporal difference for sentinel-1 acquisitions is shown in Figure 2.1.1.2. The perpendicular baseline is the difference in meters of a satellite perpendicular to its motion between the orbit of two overpasses. Due to the nature of the Side-Look-Complex (SLC) images high perpendicular baselines can cause decorrelation between pairs.

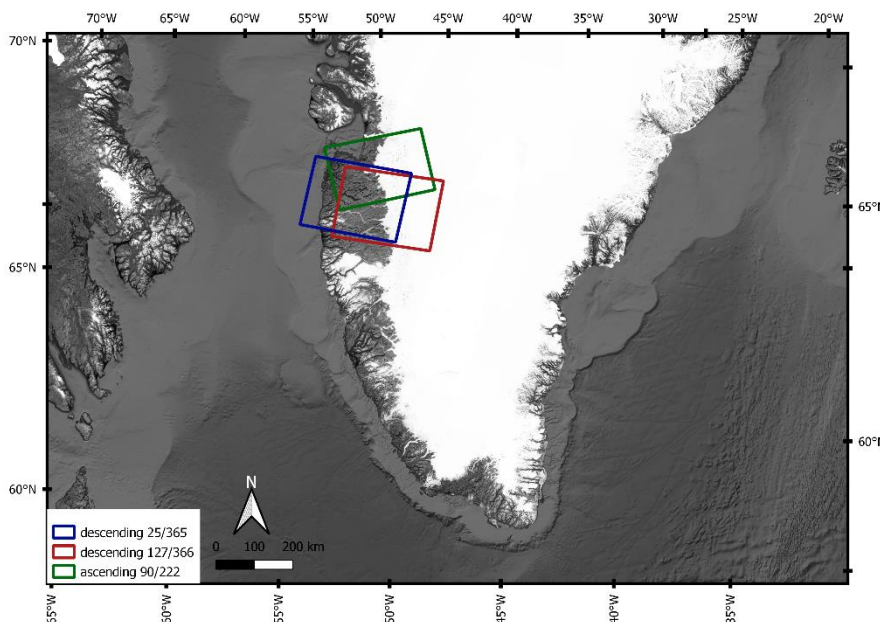


Figure 2.1.1.1 all 3 Sentinel-1 data tracks outlined over grayscale Google Earth satellite imagery with coordinates shown in WGS 84

2.1.2 Sentinel-2

The Sentinel-2 constellation consists of two optical satellites Sentinel-2A, and Sentinel-2B. The mission supplies a Top of Atmosphere (TOA) reflectance product with the Red Green Blue (RGB), Near-Infrared (NIR) and Short-Wave InfraRed (SWIR) bands in a 10 or 20m spatial resolution. The Sentinel-2 products are downloaded as level 1C radiance data and converted to level 2A Bottom Of Atmosphere (BOA) reflectance data using the Sen2Cor algorithm [Main-Knor et al., 2017]. All images used for this case study are from July, August and September of 2017, covering the pre- and post-fire cloud free images needed for the computation of the Differenced Normalized Burn Index (DNBR) and Normalized Difference Vegetation Index (NDVI).

2.1.3 DEM

A Digital Elevation Model (DEM) with high spatial resolution low error margins is needed for the computation of the interferometric phase and the non-topographic phase and displacement. The pre-processing in SNAP and the processing in StaMPS have been done with the GIMP-DEM. The spatial

resolution of the DEM is the limiting resolution in this research, resulting in a resolution of 30m. I also retrieved slope and aspect from the DEM for further analysis in relation to displacement.

2.2 PS-InSAR processing

After initial discovery of the potential of InSAR techniques for monitoring the displacements on the Earth's surface, the technique spread fast. The potential of InSAR is proven in both human-made [Delgado et al., 2018 ; Tomás et al., 2010] and natural subsidence [Joa et al. , 2003 ; Grzesiak and Milczarek, 2018]. As temporal decorrelation, the loss of compatibility between two identical pixels of two different SAR acquisitions caused by their dissimilarity in scatter over time, held back the possibilities of time series analysis; a new method was developed. The new PS InSAR techniques introduced by Ferretti et al. (2001) exploit the amplitude characteristics of pixels to determine persistent scatterers over time that can be used for interferometric analysis. PS-InSAR is a time-series Differential interferometric Synthetic Aperture Radar (DInSAR) technique, it uses the phase difference between one master SAR acquisition and all other slave images to compute the displacement. This case study uses the spatial correlation PS-algorithm of StAMPS to compute the seasonal displacement time series of a natural area. Earlier research on the 2017 Anavtavuk river fire in Alaska, USA, showed the possibilities with DInSAR for fire-induced subsidence [Iwahana et al., 2016]. The following Github [<https://github.com/gvanleeuwen/SNAP-StAMPS-Visualizing>] supplies a documentation on the installation and processing chain, a complete list of processing parameters and scripts.

2.2.1 Background on DInSAR for computing displacement

SAR images from Sentinel-1 consist of both amplitude and phase information, captured using an active radar signal to retrieve the ground backscatter. These SLC images are taken with a side look in multiple swaths and bursts (Figure 2.2.1.1), using orbit information and debursting this information can be transformed in the phase signal with a ground resolution of 10m in azimuth and 2m in range. The phase represents the absolute number of wavelengths plus the extra fraction of a wavelength it took for the signal to return to the satellite. Based on this phase fraction, which is measured to great accuracy, of two images a phase difference can be computed that consists of multiple components (equation 1).

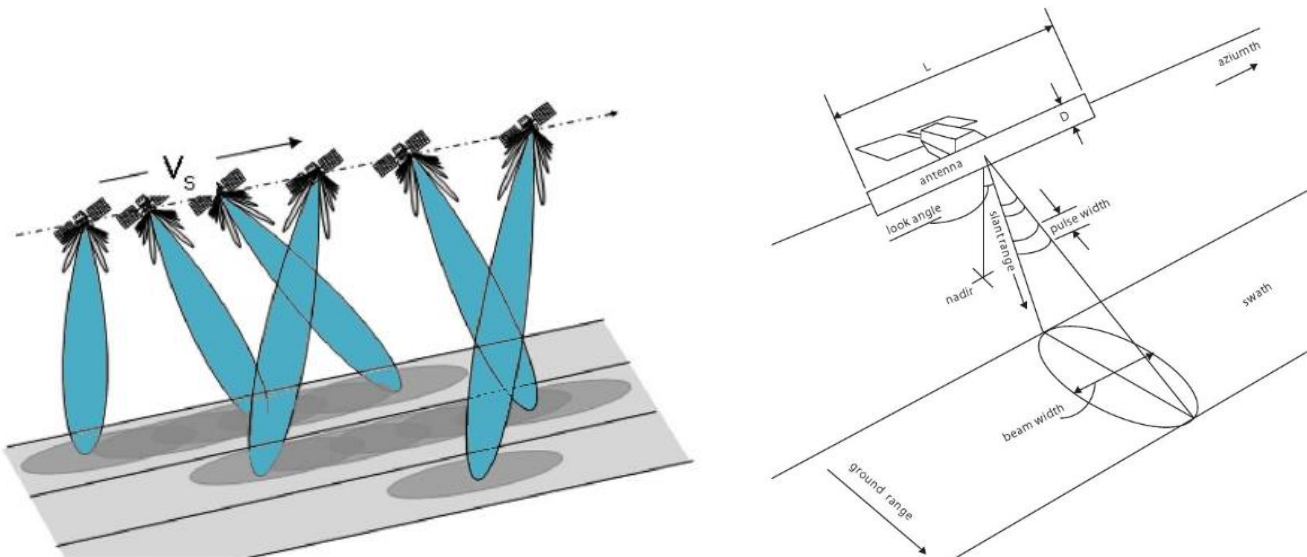


Figure 2.2.1.1 (Left) TOPS acquisition using overlapping bursts, (right) side look geometry of a SAR satellite. [De Zan and Guarnieri, 2006] and [liu et al., 2012]

The interferometric phase shown as φ_{int} is differentiated into the phase difference due to deformation, atmospheric disturbance, orbital change, topographic phase and phase noise:

$$\varphi_{int} = \varphi_{defo} + \varphi_{atmos} + \Delta\varphi_{orbit} + \Delta\varphi_{topo} + \varphi_{noise} \quad (1)$$

The deformation in the time span of the two acquisitions is just one of the signals represented in this phase difference (Figure 2.2.1.2) and a DInSAR image of 2 acquisitions is not enough to reliably model and eliminate the other components represented in the phase difference φ_{int} . The topographic phase $\Delta\varphi_{topo}$ is the contribution from the topography and earth's curvature in the phase signal and is removed using a DEM. The topography also distorts the image, since it is taken from a side look angle. This look-angle error has both a spatially correlated and uncorrelated part and is removed in StaMPS by

modelling the impact via the perpendicular baseline and spatial phase characteristics. The orbital change $\Delta\varphi_{orbit}$ is mostly visible as a ramp caused by the difference in exact orbit between the two SAR acquisitions and is removed by modelling the impact. The atmospheric phase φ_{atmos} , the difference in atmospheric conditions shortening or increasing the travel time of the SAR signal, is removed using the phase methods of the TRAIN toolbox. The components which remain in the signal are the phase noise φ_{noise} and deformation phase φ_{defo} . The phase noise is partially removed using filtering but is never fully eliminated. A time series of multiple images is needed to show certain displacement patterns and eliminate these spatial and non-spatial error elements in the phase difference. Temporal decorrelation is common in DInSAR and has many sources like atmospheric disturbance but mostly landcover change. These phenomena change the phase sum of a pixel incoherent with possible deformation signal, decorrelating 2 SAR acquisitions and leaving them unusable for standard DInSAR. Ps-InSAR diminishes temporal decorrelation by using pixels with objects that dominate the phase sum due to a high amplitude, so called Persistent Scatterers (PS) (Figure 2.2.1.3). StaMPS uses a spatial correlation algorithm that also greatly

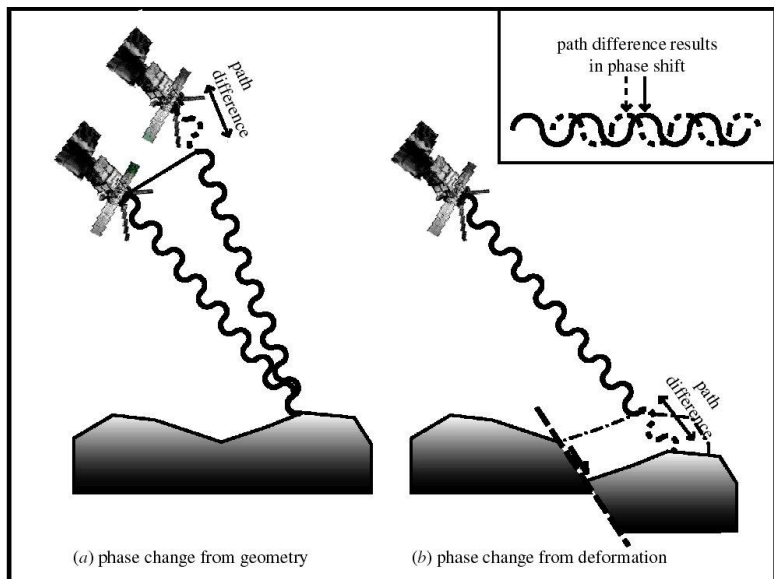


Figure 2.2.1.2 An active SAR signal is represented as the phase in the images. When deformation happens, the phase is different which gets picked up by the next overpass. The phase difference between these 2 passes is used to calculate this deformation.

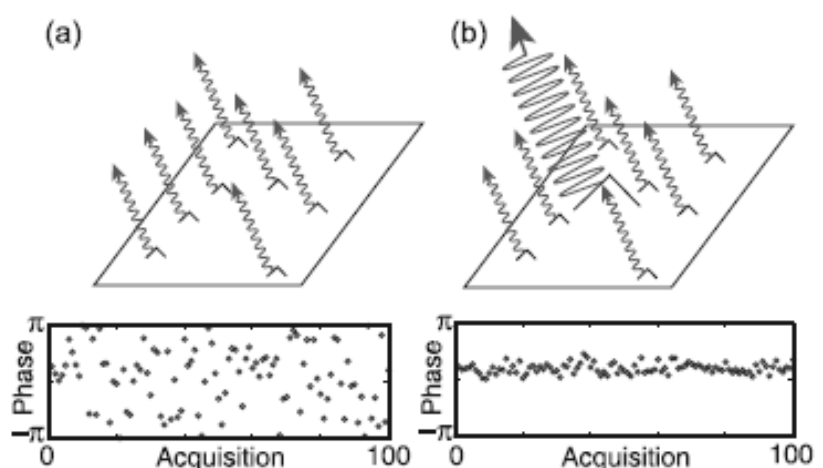


Figure 2.2.1.3 The difference between a non Persistent Scatterer (PS) (a) and a PS pixel (b) [Ferretti et al., 2001]. The high amplitude ground scatterer from image b causes the phase sum to be more consistent over time remedying temporal decorrelation.

improves the amount of PS selected in natural areas. After removing the topographic phase using a DEM the flat earth phase interferogram is filtered with a Goldstein filter before unwrapping the result [Goldstein and Werner, 1998]. A Goldstein filter is a kernel-based operator that filters the phase difference based on the filter strength alpha, generally between 0.7 and 1.0 in strength, and the estimated phase in the window based on spatial correlation. The unwrapping of the phase difference is translating the multiple ambiguous phase differences from all the slaves in relation to a single master into the respective displacement in radians. The Line Of Sight (LOS) displacement in radians is converted into vertical displacement by using equation 2 which is derived using the acquisition geometry (figure 2.2.1.4) and assumes only vertical displacement.

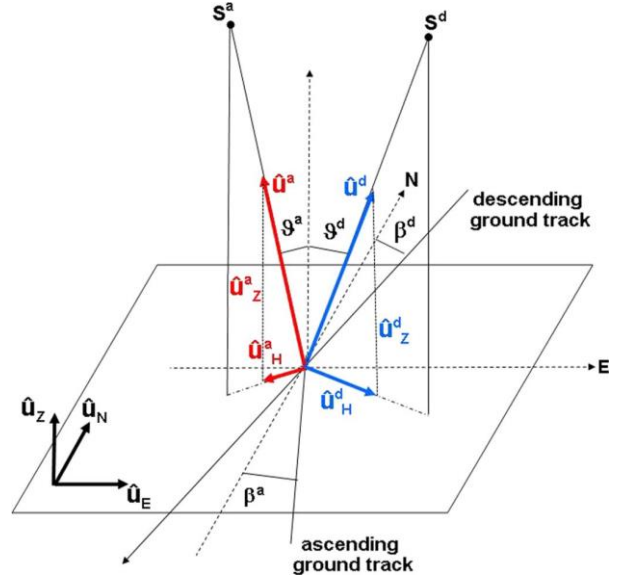


Figure 2.2.1.4 acquisition geometry of the ascending and descending SAR tracks, most important is the incidence angle, shown as ϑ and the difference between the vertical and the LOS.

Vertical Displacement: formula for calculating the D_{vert} based on the incidence angle and D_{LOS} , assumes only vertical displacement and is less accurate when only using data from 1 track:

$$D_{vert} = \frac{D_{LOS}}{\cos(\text{rad}(\vartheta_{\text{incidence}}))} \quad (2)$$

The LOS displacements and velocity information from StaMPS is exported to a Comma Separated Values (CSV) file and imported into a Python environment for calculation. The three data tracks show different displacement results because of their flight direction and orbital difference in both space and time. Therefore, the vertical displacement velocities from all three tracks are combined by calculating the mean displacement of a pixel. The final mean displacement velocity is only computed for pixels that have a value in the ascending and one of the descending tracks. If the point has values in all 3 tracks the descending value is the mean of both descending tracks. The final displacement result should always be considered relative when no ground measurements are integrated, even when selecting a good reference point.

2.2.2 Pre-processing using SNAP

The red processing steps in Figure 2.2.2.1 show the workflow in SNAP using the Snap2StaMPS Python wrapper package. SAR images are first corrected for their exact orbit and clipped to the AOI to be able to compare the images. All images were oversampled from a resolution of 10 meters in range and 2 in azimuth to a resolution of 20 meters in range and 5 in azimuth. The SNAP software is then used to coregister, resample one image to the same ground pixels of the second observation, all slave images to the single master which, is chosen by minimizing the temporal and perpendicular baseline (Figure 2.1.1.2). After coregistration the interferograms for each image pair are formed

which, shows the phase difference in continuous phrings. The topographic phase and phase due to the Earth's curvature are removed with height data from the GIMP-DEM. The data is then exported into the correct file structure for StaMPS.

2.2.3 Processing using StaMPS

Starting the processing in StaMPS the initial PS are selected with a formula for selecting based on the amplitude dispersion threshold which, determines phase stability [Ferretti et al., 2001] (equation 3). The lower the threshold the stricter the PS will be selected. The preparation script, ran in a Linux terminal, is dependent on the pre-processor used and prepares the data for further analysis in the Matlab environment of StaMPS (Figure 2.2.2.1).

The Amplitude dispersion threshold D_A determines the amplitude standard deviation and mean amplitude ratio threshold for a PS pixels and is a measure for phase stability:

$$D_A = \frac{\sigma_A}{\mu_A} \quad (3)$$

First steps in the Matlab processing is setting the parameters using the *setparm* command. Important parameters are shown in the Github and in more detail in the StaMPS manual [Hooper et al., 2018]. Based on the parameters set, StaMPS will load the data in step 1 and estimate the phase noise with the Combined Low-pass and Adaptive Phase (CLAP) filter [Hooper, 2007; Sousa et al., 2011] in step 2. In step 3, pixels with high phase noise will be dropped based on buffer sizes and threshold values for spatially correlated phase jumps. More noisy pixels will be removed in step 4 based on their standard deviation and ground scatter contributions. After merging the processing patches set earlier in the process, resampling the point data to a grid and calculating the spatially uncorrelated look-angle error, the phase difference will be unwrapped in step 6. StaMPS uses SNAPHU 3D unwrapping [Hooper and Zebker, 2007] to convert the phase difference into LOS displacement values for each image pair. After running step 7, which estimates the spatially correlated look angle error, step 6 can be run again with first removing the errors calculated in step 5 and 7 to improve the unwrapping process. After completion of the StaMPS steps, the linear atmospheric correction of TRAIN is computed to improve the results. Using the *pt_plot* function of stamps the LOS displacements can be displayed including their standard deviation and time series plots.

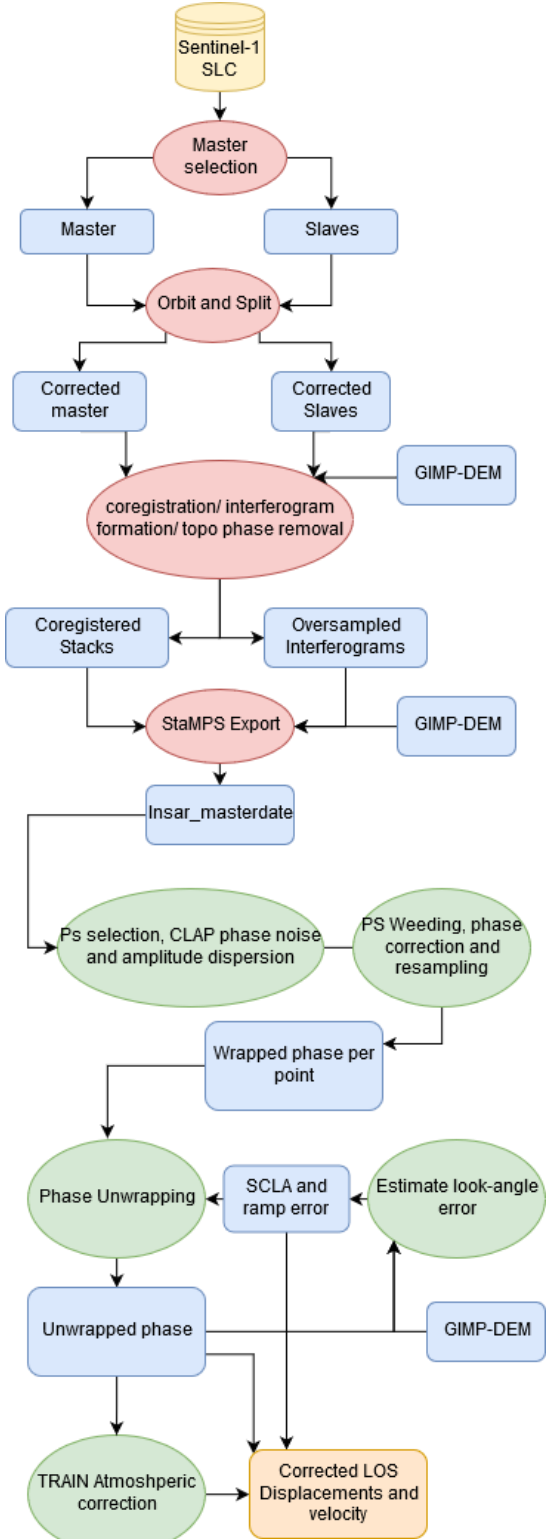


Figure 2.2.2.1 Processing chain in SNAP(red) and StaMPS(Green). All processes are shaped like an oval and input data is square.

2.3 Analysis of environmental drivers of subsidence

The mean displacement velocity of both years was analysed in relationship to multiple environmental proxies, greenness by NDVI, fire severity by DNBR and aspect and slope. All data layers were re-projected into the Universal Transverse Mercator (UTM) zone 22N/W projection (EPSG: 32622). The Sentinel-2 images used for computation of the different indices were downloaded

[<https://scihub.copernicus.eu/>] in TOA level 1C products and converted into BOA reflectance using the Sen2Cor algorithm. The aspect and slope maps were generated, using the 30m resolution GIMP DEM that was also used for InSAR processing. The NDVI image was computed using equation 4 on a Sentinel-2 image with a spatial resolution of 10m. After computing the NDVI at 10m resolution the image was spatially averaged to a 30m resolution for later processing. The NBR images (equation 5) of the earliest dates pre- and post-fire without clouds above the AOI were used to compute a DNBR image following equation 6. The Short-Wave InfraRed (SWIR) band shown in the equations is the 12th band of the Sentinel-2 data, with a band centre of 2190nm, in a 20m resolution. The Near-InfraRed (NIR) band of Sentinel-2 is the 8th band with a band centre of 842nm and is provided in both 10- and 20m resolution. The DNBR image is later categorized based on a common classification shown in table 2.

Normalized Difference Vegetation Index (NDVI) [Roush et al., 1973] uses red and infrared bands to represent the amount vegetation greenness. High values represent high and greenness while lower values represent areas with sparse or no vegetation:

$$NDVI = \frac{NIR - RED}{NIR + RED} \quad (4)$$

Normalized Burn Ratio (NBR) [Zhu et al., 2006] computed for both pre- and postfire and is in values between -1 and 1 with low values being burn scar or bare ground and values > 0.2 as vegetation

$$NBR = \frac{NIR - SWIR}{NIR + SWIR} \quad (5)$$

Differenced Normalized Burn ratio (DNBR) [Lopez Garcia et al., 1991 ; Key and Benson, 1999] represents a proxy for fire severity as it is the change in how burned an area is. (Figure 3.2.2)

$$DNBR = NBR_{prefire} - NBR_{postfire} \quad (6)$$

Class	DNBR- fire severity	severity
1	< 0.0	Enhanced regrowth
2	> 0.0 and < 0.1	Unburned
3	> 0.1 and < 0.27	Low severity
4	> 0.27 and < 0.66	Moderate severity
5	> 0.66 and < 0.8	High severity
6	> 0.8	Extreme severity

Table 2 showing the DNBR classification for environmental analysis.

The computed indices are evaluated in relation to the mean displacements of 2016 and 2018. The analysis was performed in Python and uses mostly the Gdal and NumPy libraries. The process selects a subset of pixels of the image based on a polygon of the area of interest (AOI). The script is parsed two raster layers, one layer with displacement values and one with the environmental variable. The script then compares the displacement values for every pixel with the respective environmental value on the same location. I aggregated displacement values in classes based on classes of the environmental variables. For some relationships, regression lines were calculated using the SciPy

library. To normalize the change of the displacement between 2016 and 2018 in the burned area, I compared the burned area difference to the 2016 – 2018 difference in the unburned area (equation 7).

Displacement difference normalized: shows the normalized change from old to new in the burned area in comparison to the unburned area. All values are mean relative vertical displacement velocities in mm/year

$$Ddiff_{normalized} = D_{2018burned} - D_{2016burned}) - (D_{2018unburned} - D_{2016unburned}) \quad (7)$$

3. RESULTS

The displacement results shown in figure 3.1.1 are discussed in chapter 3.1 and comparative results shown in chapter 3.2. The spatial resolution off all analysis was 30m and analysis were performed in UTM zone 22N/W projection. All displacements results were referenced for the point in figure 3.2.3.

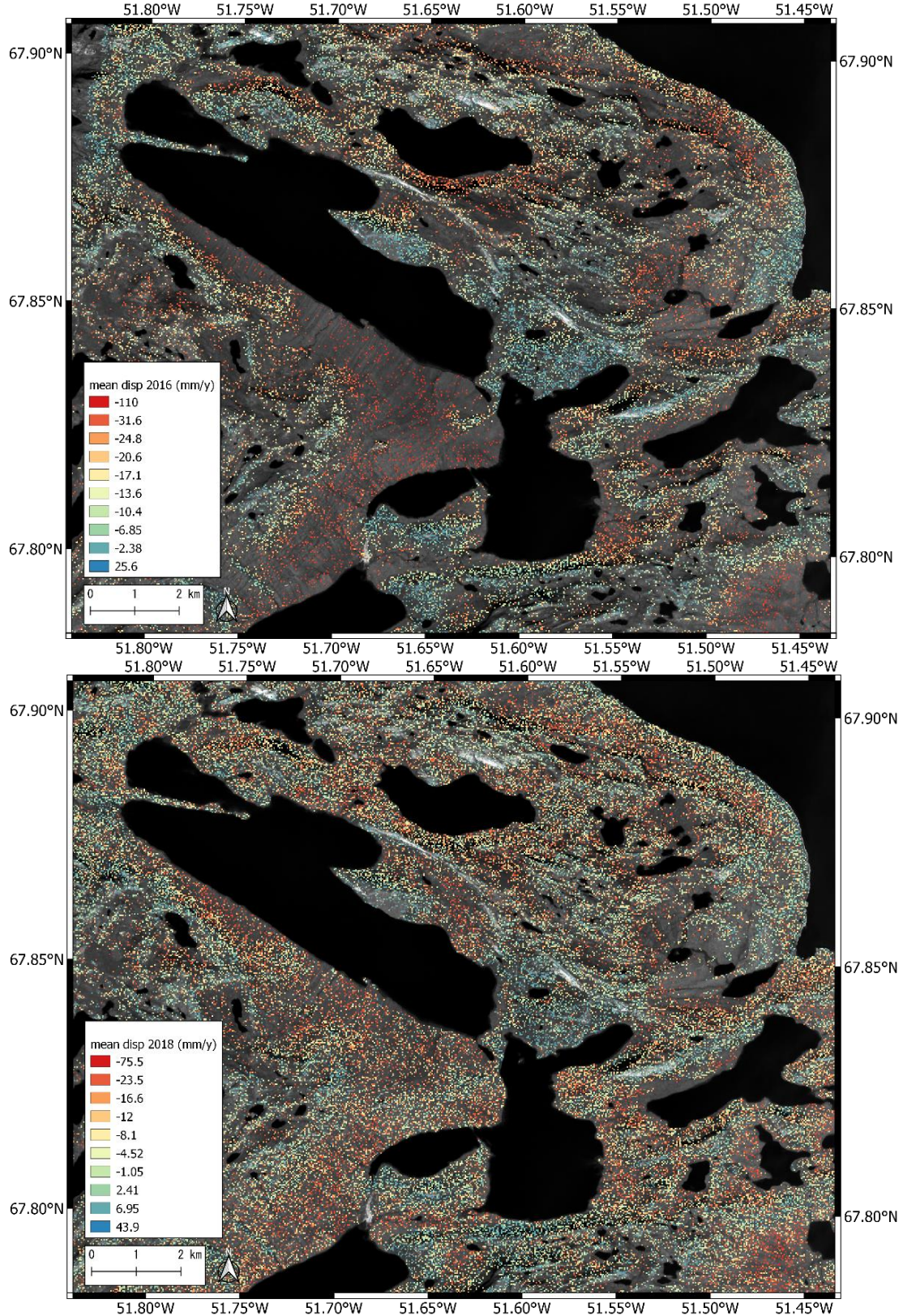


Figure 3.1.1 The mean vertical relative displacement velocities for 2016 and 2018 shown in the figures above are computed with 9 and 20 interferograms respectively for 2016 and 2018. The coordinates are given in WGS84 and the classification is in 10 quantiles.

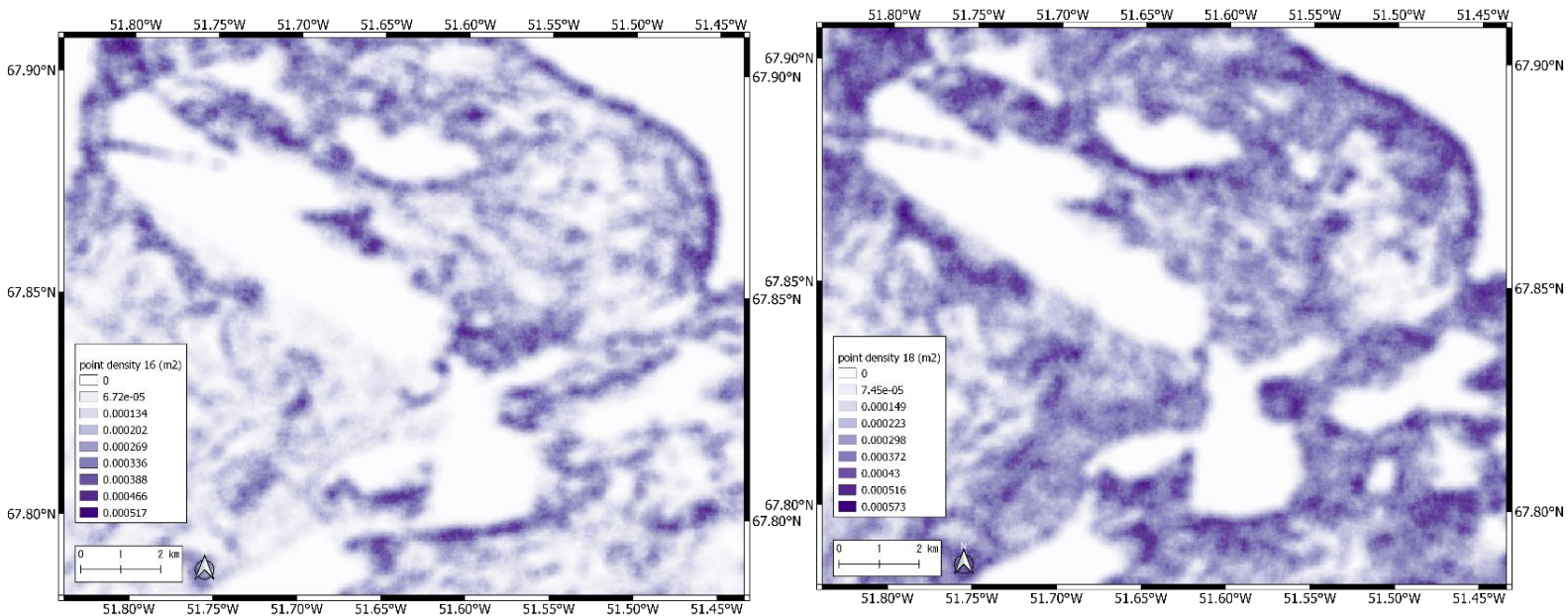


Figure 3.1.2 PS point density in points/m² for both 2016(left) and 2018(right), calculated over a 200x200m area colour coded using 10 quantiles.

3.1 PS-InSAR

The vertical displacement velocities shown in Figure 3.1.1 for 2016 and 2018 both have a different amount of acquisitions used because Sentinel-1B was not operational for this area yet in 2016. The mean displacement velocity in the AOI for 2016 is -16.8 mm/year and for 2018 is -7.6 mm/year with a mean velocity standard deviation of 10.65 mm/year and 8.85 mm/year respectively. This standard deviation is a measure of error for the linear regression line through the time-series that represents the velocity, the mean is generated over the complete area of interest. The velocity output from StaMPS is a linear relation through the time-series plot for each point given in mm/year and does therefore not reflect the absolute displacement in the timespan of the data. All displacements shown should be seen relative and not absolute because no absolute reference point was available and because the InSAR results differ over greater distance due to uncorrected atmospheric and topographic contributions. The displacement data should be interpreted as differences between areas; therefore, we cannot make concrete statements about uplift or subsidence, especially in areas close to zero displacement. The mean displacement velocities for both 2016 and 2018 have less data points than the displacement maps per track, because of the way the mean is generated. The amount of PS points for 2016 and 2018 are 37157 and 61437, and the point density differs greatly between the two years (figure 3.1.2). The years do not have roughly the same PS points since the amount of acquisitions used for computation is higher in 2018. The pattern in the mean displacement velocities of 2016 (Figure 3.1.1) seems smoother, has more difference between the minimum and maximum and is characterized by high relative subsidence in the southeast, west of the middle and in the middle of the north eastern quadrant. Relative uplift seems to occur near the north eastern coasts, the inland coastline and the south and western part of the AOI. The pattern in 2018 has more spatial variability that can seem noisy at places; although the standard deviation is lower. The minimum and maximum of 2018 show the same lowering trend as the mean displacement for the complete displacement, with a maximum velocity difference of 119,9 mm/year. The standard deviation maps (Figure 3.1.3) show spatial correlations in uncertainty and present a range for the standard deviation from 1.5 to 24 mm/Y in 2016 and from 2 to 28.5 mm/Y for 2018.

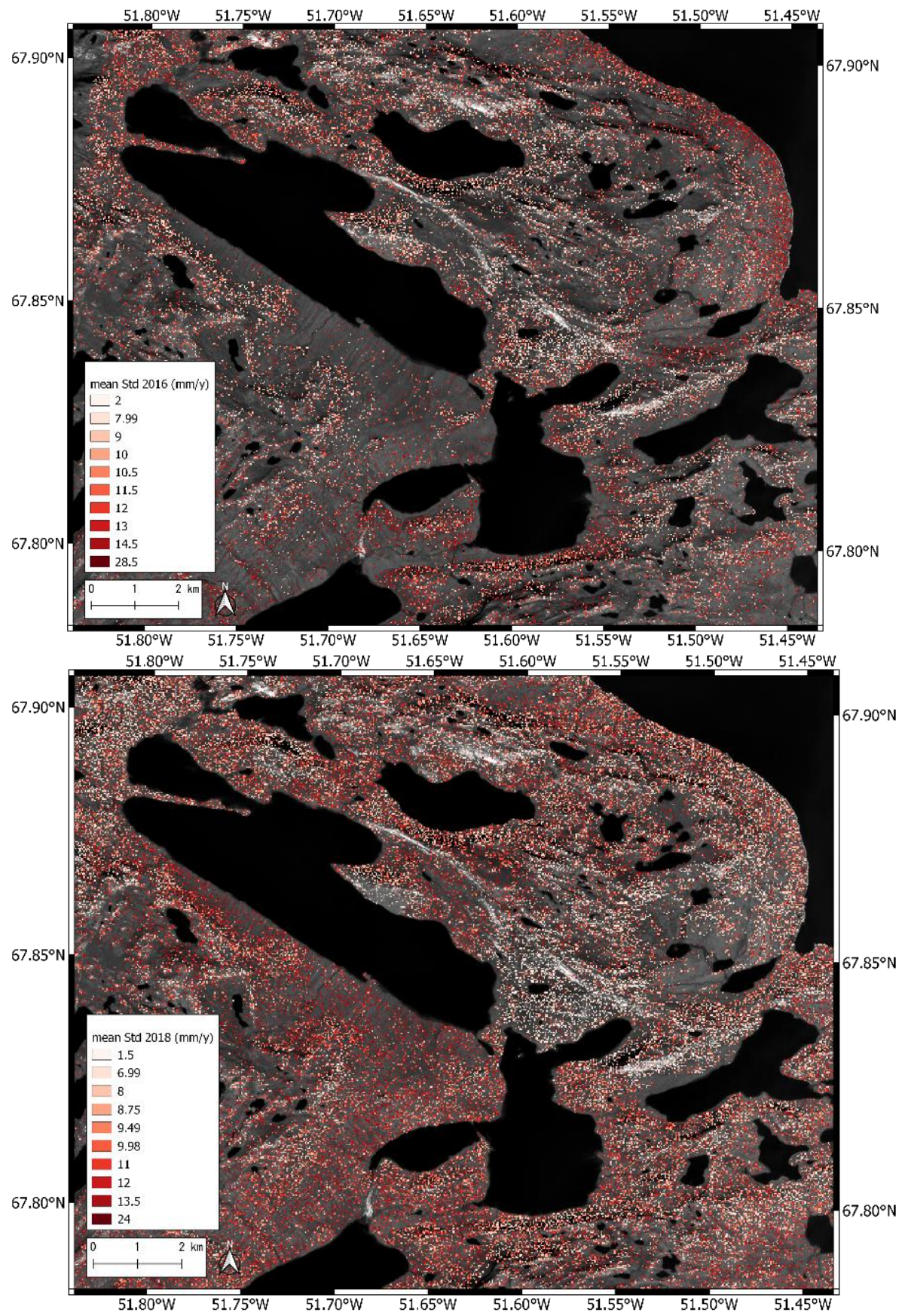


Figure 3.1.3 The mean standard deviation for the 2016 and 2018 PS-INSAR velocities. The standard deviation is a measure for the error along the linear relationship in the time-series for every point that represents the velocity. These results are also corrected for the computation of vertical displacement and are presented in 10 quantiles.

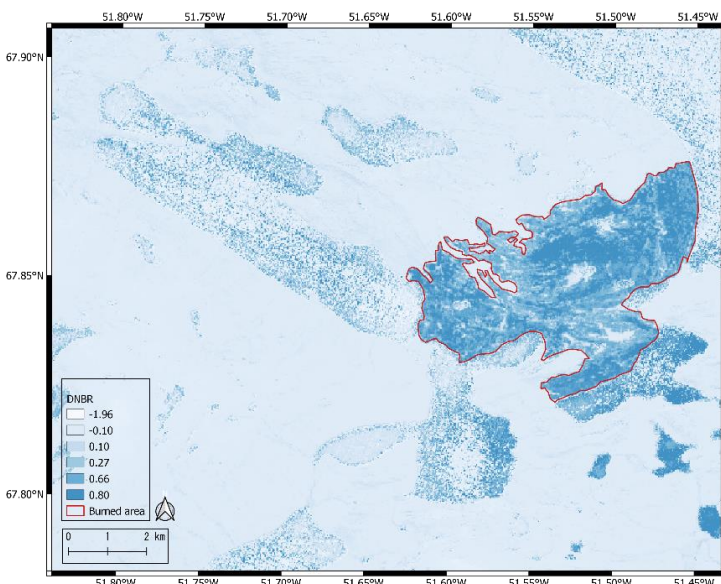


Figure 3.2.1 The fire severity for the 2017 Greenland fire as computed from the Sentinel-2 acquisitions 20170726 and 20170904. All burned area is within the red line and results outside of this burn line are

3.2 Environmental drivers

To inspect the effect of the 2017 tundra fire the displacement results were compared with different environmental variables. In the discussion, questions are raised for further analysis. Except for the aspect, height and slope, these analyses will be specifically for the burned area shown as red line in Figure (3.2.1). The environmental variable greenness is shown in figure 3.2.2 and the topography variables are shown in figure 3.2.4 in section 3.2.2

3.2.1 Displacement in relation to fire severity and greenness

The fire severity was highest in the middle, north eastern, southern and north western part of the area (Figure 3.2.1). A possible relation between the fire severity and subsidence rate can only be based on the 2018 data, since the fire scar was created in 2017 and the data of 2016 therefore show no fire impact. The annual weather variability also limits the comparison options between the pre- and post-fire subsidence. Visually it is difficult to find a strong spatial correlation between the fire severity and the displacement difference (Figure 3.2.1.1), the more severe areas seem

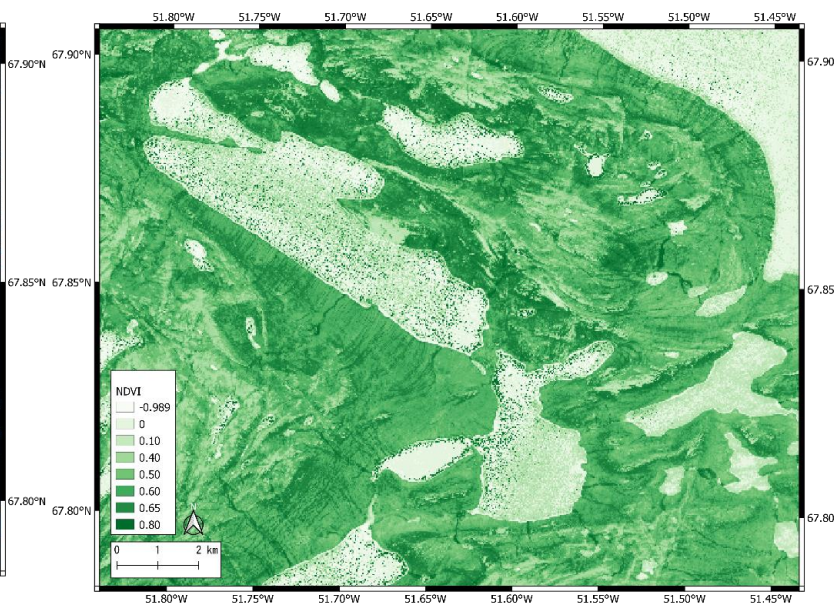


Figure 3.2.2 The normalized difference vegetation index as computed from the Pre-fire Sentinel-2 acquisition 20170726 showing vegetation greenness

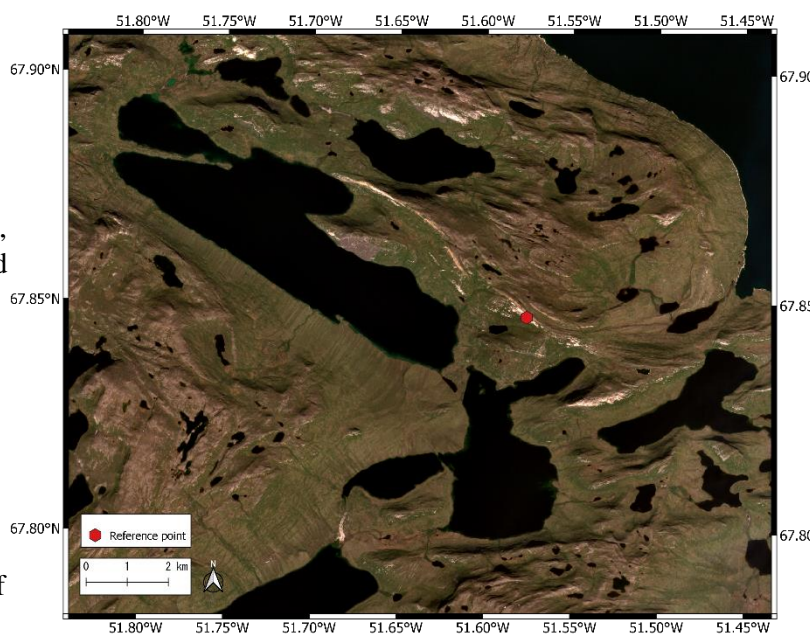


Figure 3.2.3 Sentinel-2 image of 20170726 in true colour composite with a red Hexagon point showing the location of the reference point for displacement values.

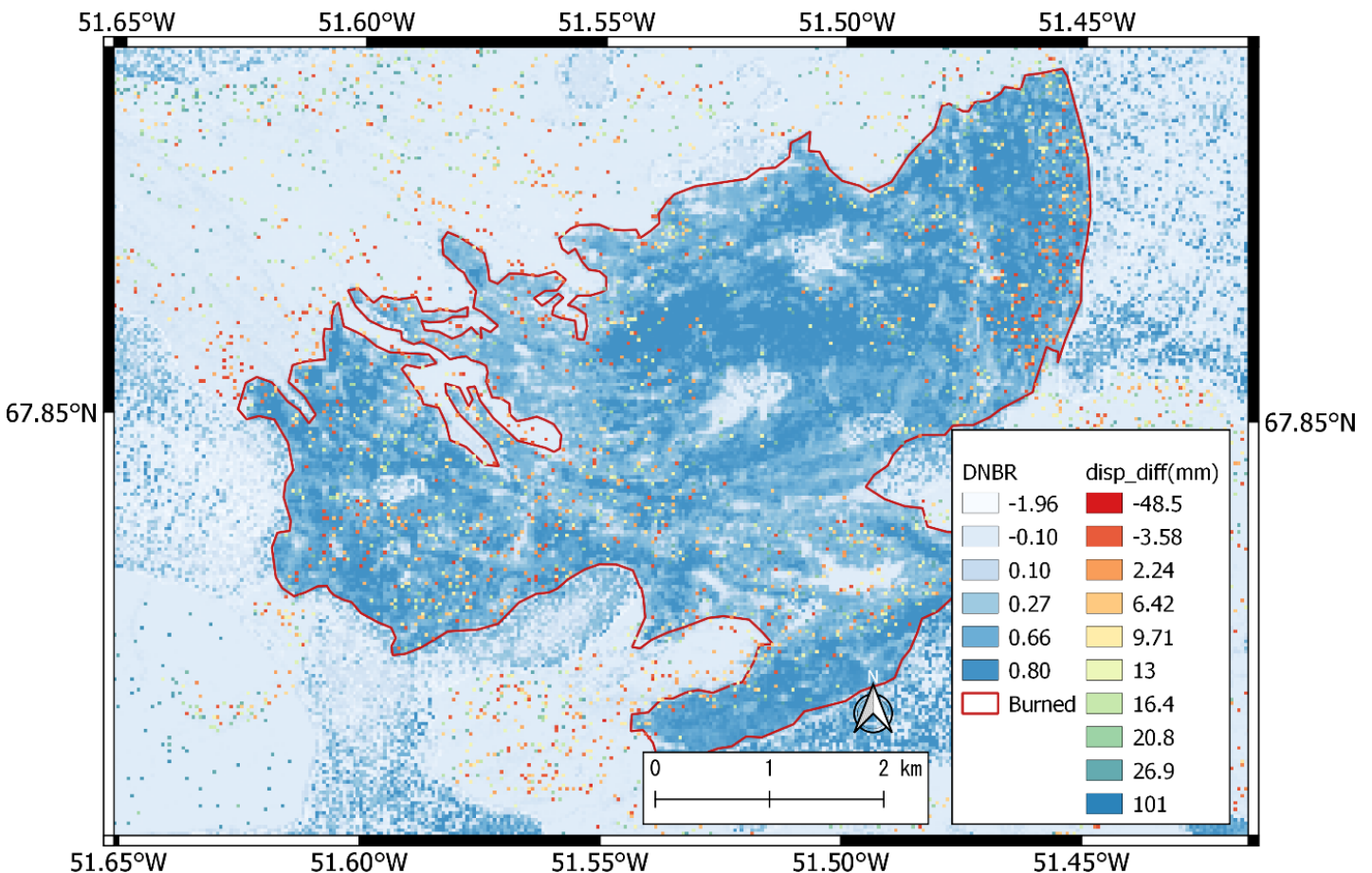


Figure 3.2.1.1 Deformation difference between 2018 and 2016 in relation to the fire severity. Only pixels which have values in both 2016 and 2018 are used. The red outline shows the fire scar with darker blue values having a higher fire severity.

to have less PS points and have more relative subsidence though. Using aggregate statistics based on thresholds it is easier to see possible relations between the fire severity and displacement velocity. Figures 3.2.1.2 and 3.2.1.3 show the relation of the fire severity of the 2017 fire to the displacement velocity in the upcoming thaw season 2018. The displacements aggregated over 6 different fire severity classes are shown in Figure 3.2.1.3, the bars seem to show a small non-linear trend from -2.5 to -4 mm/Y. Subsidence increased linearly with fire severity (Figure 3.2.1.2). The slope of the regression line was small, yet significantly different from zero ($p = 0.047 < 0.05$). This analysis only considered data points with a standard deviation in subsidence of less than 10 mm per year, a NDVI lower than 0.1 and a DNBR lower than 0.1. The displacement differences from 2016-2018 in relation to the DNBR fire severity are shown in Figures 3.2.1.4 and 3.2.1.5. the scatterplot shows a possible trend with a R^2 of 0.0025 and a P-value of 0.20. The bar plot in Figure 3.2.1.5 shows a negative trend of ~3.5 mm/year difference except for the “low” class. The mean displacement velocities of 2016 and 2018 are both aggregated over the burned and unburned area, the results are shown in table 3. The difference between the burned area- and unburned area difference over 2016-2018 is -4 mm which suggests the burned area displacement changed more negative than the unburned area. This minor difference is also reflected in the burned – unburned statistics, which shows the positive difference between burned and unburned has decreased from 2016 to 2018 and suggests more displacement in the burned area in 2018 in comparison to 2016.

	Burned	Unburned	Burned - unburned
2016	-10.75	-15.79	5.04
2018	-2.90	-4.95	1.05
2018-2016	6.85	10.85	Disp vel (mm/Y)

Table 3 shows the aggregated mean displacement over the burned area polygon for fire severity >0.1 in column burned and the complete AOI without the burned area for the unburned column. Difference shown in row 2018-2016 show more difference for the burned area than for the unburned.

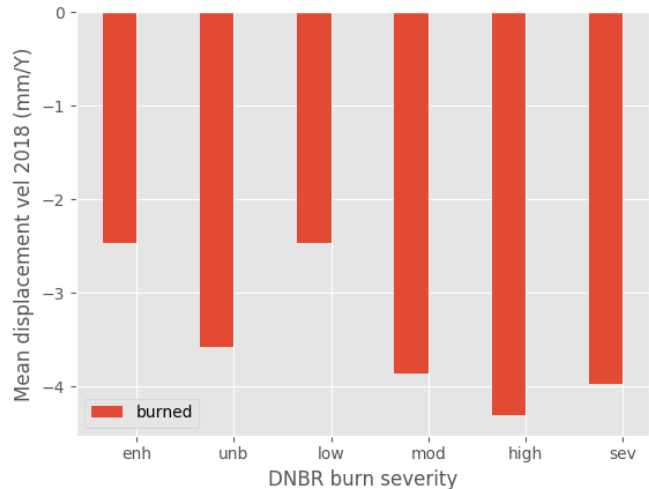
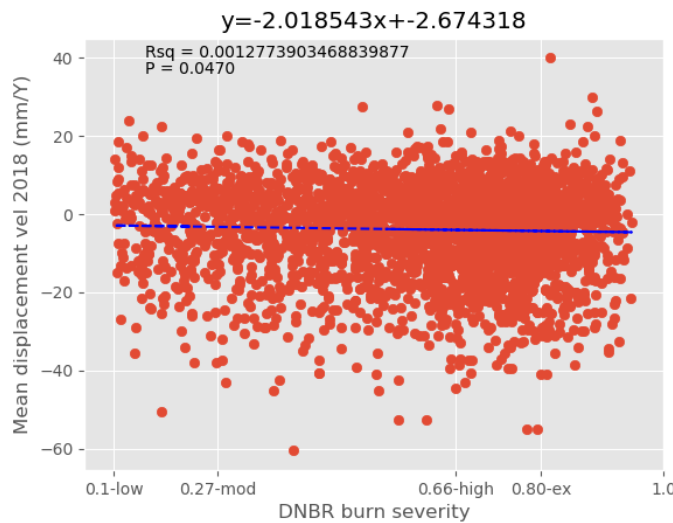


Figure 3.2.1.2 and 3.2.1.3 showing the relation of the displacements of 2018 with the DNBR fire severity. All points used for this analysis are sorted for a NDVI >0.1 and a STD < 10 within the burned area polygon to exclude areas without topsoil or too much uncertainty. The classes in the bar plot are divided as shown in the methods section.

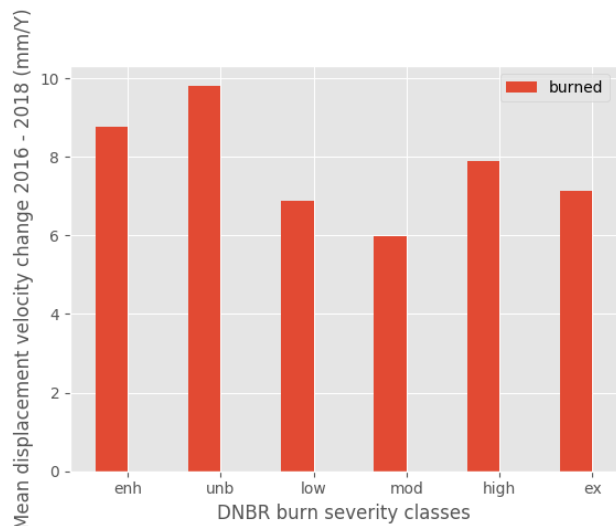
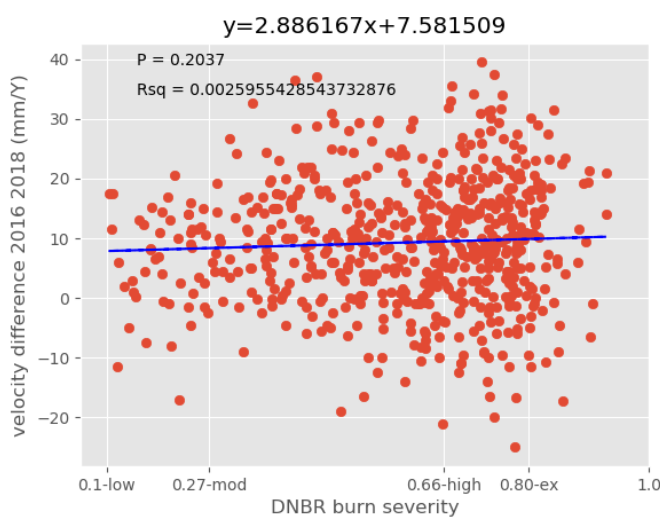


Figure 3.2.1.4 and 3.2.1.5 showing the relation between the velocity difference over 2016 and 2018 with the DNBR fire severity. The scatter plot (left) shows points aggregated over the burned area polygon for each point which is available in both 2016 and 2018 with a NDVI > 0.1 and a STD < 10. The bar plot (right) is computed by subtracting the means of each class for 2016 and 2018 for the same thresholds as the scatterplot.

The bar plot in figure 3.2.1.6 shows a possible negative trend between the greenness and the displacement velocity. In Figure 3.2.1.7 the same relation is shown as a positive trend of +0,0014 (mm/y)/NDVI with a R^2 value of 3.8×10^{-10} and a p-value of 0.998, a non-existent trend. Visually comparing the NDVI results with the displacement shows no clear spatial patterns. Both the greenness and fire severity trends and differences are on a sub-cm scale with a high p value and are therefore not statistically significant with the variation in the velocity data. The scatterplot in Figure 3.2.1.8 shows the relation between the DNBR and NDVI image with a R^2 value of 0.083 and a p-value of 0.0 this linear trend is significant and directly links fuel to fire severity.

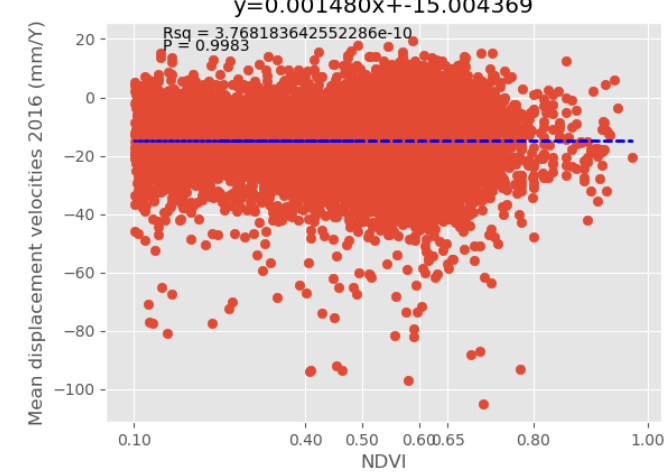
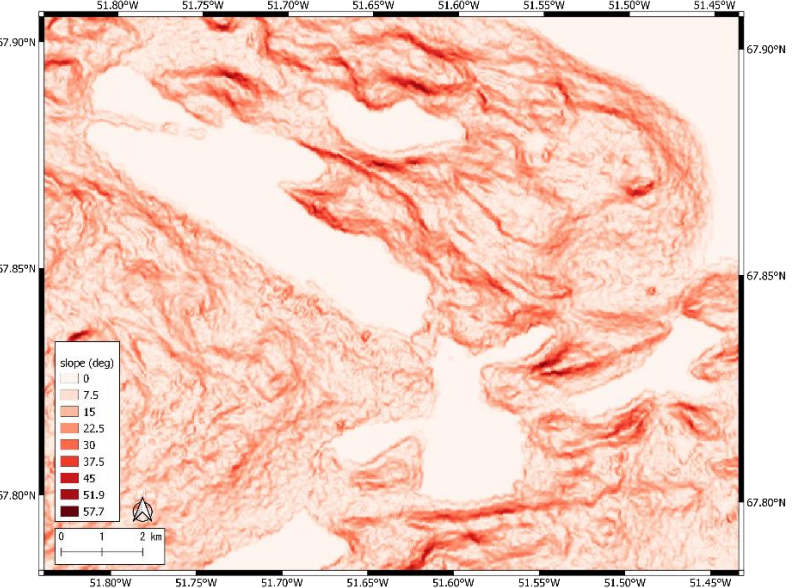
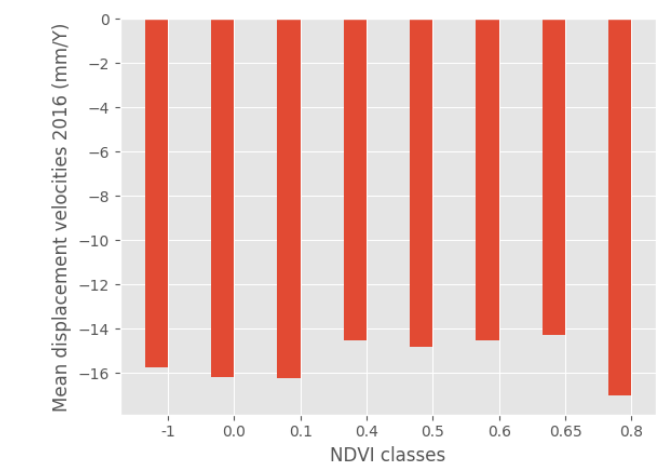
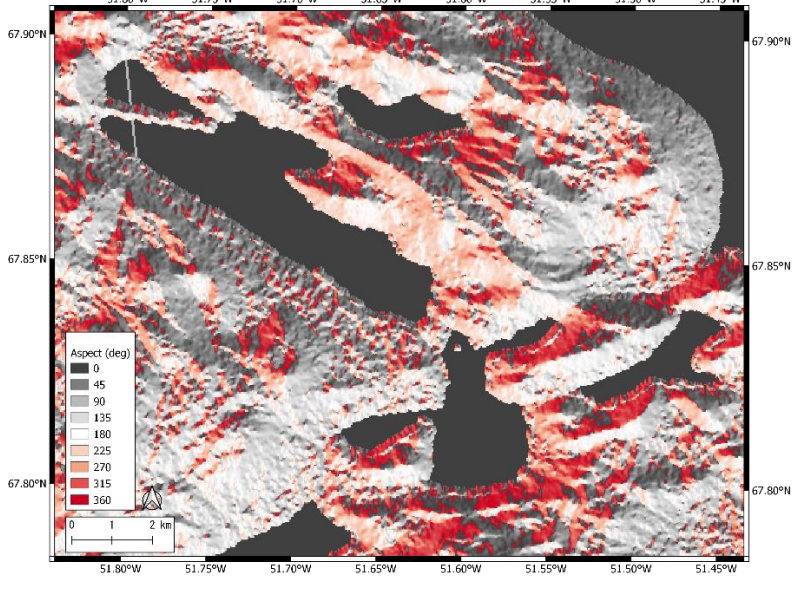
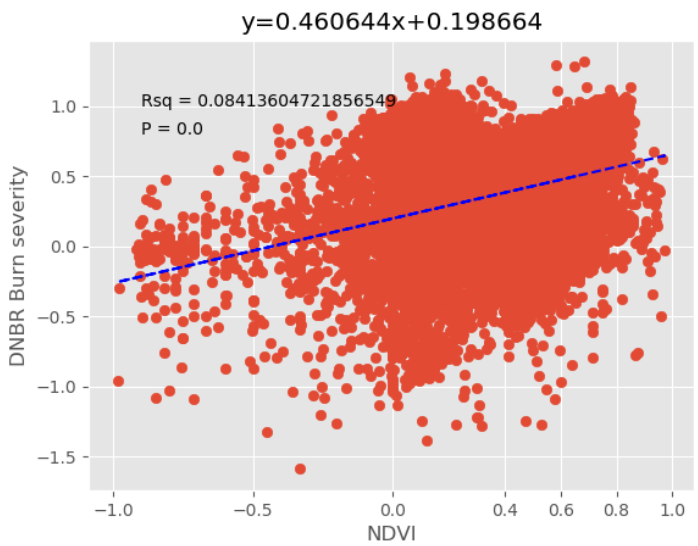
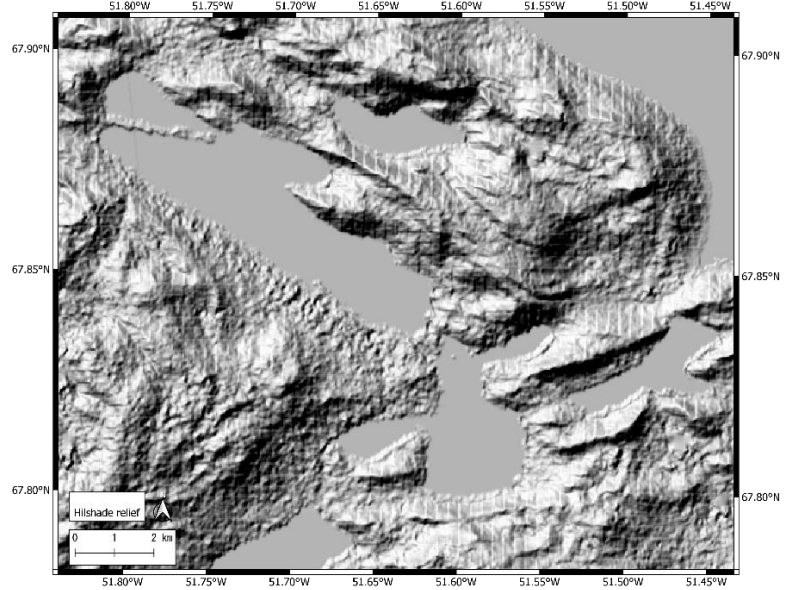


Figure 3.2.4 shaded relief, aspect and slope map (top to bottom) generated from the 30m spatial resolution GIMP DEM. Maps only used for further analysis in

Figure 3.2.1.6 (middle-bar) and Figure 3.2.1.7 (bottom – scatter) show the relation between the pre-fire NDVI and the mean relative vertical displacements of 2016 in both bar and scatterplot for the complete AOI. In the scatterplot only points with $NDVI > 0.1$ are shown.

3.2.2 Displacement in relation to relief

All relief related comparisons are done to not only directly compare the relief to the displacements but also have an indirect relationship with the surface geology. Judging from the Sentinel-2 image in Figure 3.2.3 and the topography maps in Figure 3.2.4 there are outcrops of bedrock in the AOI that are mostly in higher altitude areas. Areas with more vegetation and therefore thicker ground cover are located in lower altitude regions. The relief could therefore be an indirect relation to surface geology and the possible thickness of the active layer and therefore show the possible maximum subsidence, which is higher in areas with thicker soils. Figure 3.2.2.1 shows an inconsistent trend from -1 mm/Y tot maximum ~1.5 mm/year based on a height difference over 6 steps from 0 to 680 meter. This positive relation is also shown in the scatterplot in Figure 3.2.2.2. 0.0053 mm/year more relative displacement is a maximum difference of 3.5 mm/year displacement based on the height difference. The R² value of 0.0041 and p-value of 1.04 show this trend is not statistically significant. Figures 3.2.2.3 and 3.2.2.4 show the slope and aspect computed from the same DEM as the height data in relation with the displacement. The slope seems to have no trend with the displacement values while the aspect shows minor differences between the different directions. In general, the north facing hills have more negative relative displacement in comparison with the displacement of the southwestern and south eastern hills to a maximum difference of around 3 mm/year.

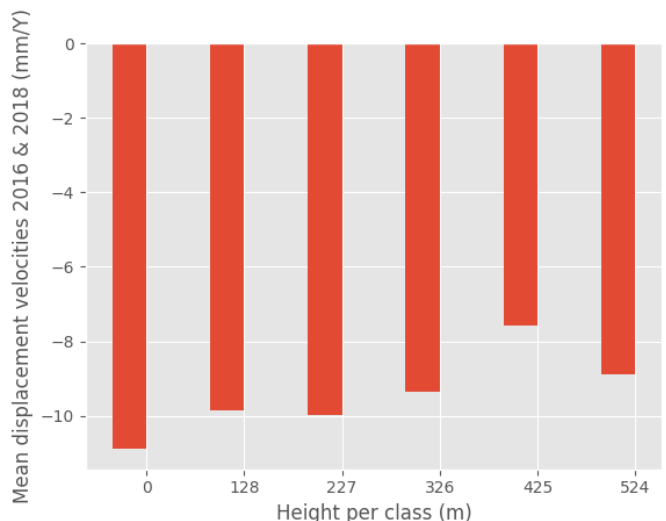
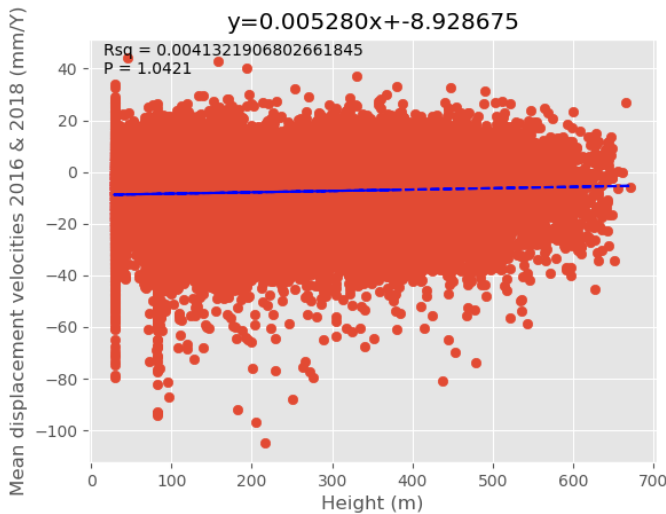


Figure 3.2.2.1 and Figure 3.2.2.2 show the relation between the height and mean relative vertical displacement velocities of both 2016 and 2018. This is computed for the complete AOI since it is not specific for burned area.

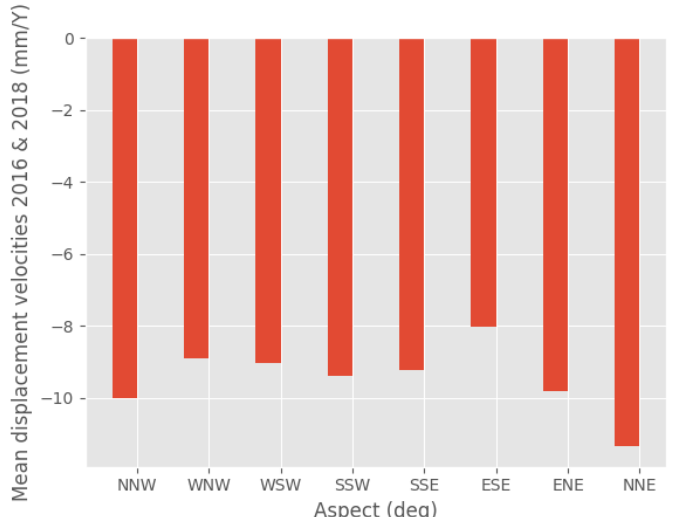
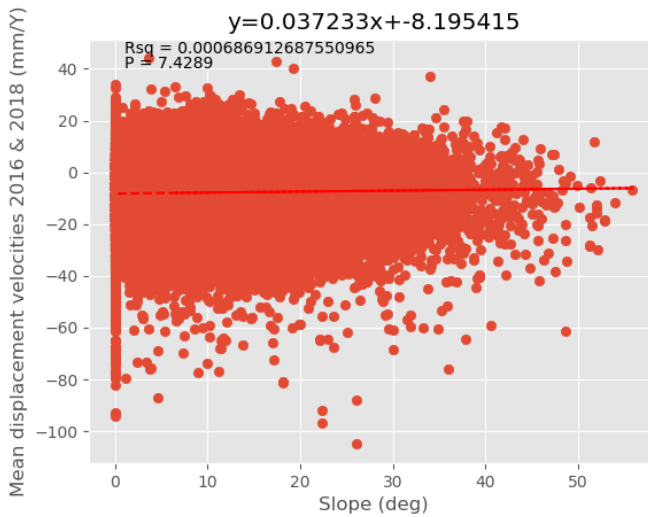


Figure 3.2.2.3 and Figure 3.2.2.4 show the slope as scatterplot and aspect as bar plot in relation to the mean displacement velocities for 2016 and 2018 aggregated over the complete AOI.

4. DISCUSSION

4.1 PS-InSAR complications and possibilities

The InSAR derived displacement velocities confirm the utility of this technique with Sentinel-1 imagery with frequent revisits for monitoring of seasonal subsidence over natural areas. Prior studies have shown mm precision with smooth temporal and spatial results and a relatively high PS-density [Hooper et al., 2007]. In this case study, this high precision may not be achieved due to a small time-series, high atmospheric disturbance and lack of a ground reference point. The mean displacement velocities computed for 2016 are plausible results with smooth temporal and spatial characteristics as expected from a continuous permafrost [Streltskiy et al., 2015]. The standard deviation for the 2016 displacements ranges from 1.5 to 24 mm/year and has a mean of 10.65 mm/year over the complete AOI. Since only 9 interferograms have been used to calculate the 2016 displacements the deviation in this data is reasonable and shows the potential for time-series analysis for seasonal subsidence over permafrost terrain, that has already been shown for DInSAR by Iwahana et al., 2016 and Liu et al., 2014. The relative mean displacements data computed over 2018 are less smooth both temporally and spatially than the 2016 results. The range in the standard deviation for the 2018 data is between 2 and 28.5 mm/year with a mean of 8.85 mm/year. These error margins again show the capabilities of the methods used and show the improvement in accuracy when using twice as much SAR acquisitions. Using more restrictive error thresholds the PS-density can be brought down to improve the overall accuracy of the used points.

Some of the processing steps of the workflow require human intervention and stochastic computer analysis, which may introduce biases in the analysis. Without an absolute ground reference point, the selection of a stable area is prone to error. The negative and positive signs therefore are not directly reflecting whether the area subsides or lifts up. The quality of the computed displacements is mostly dependant on the SAR data, DEM data and computational algorithms but to some degree also on the knowledge and expertise of the processor. The DEM data, which is also important for the quality of the interferometric phase difference calculated as shown in the methods section, is chosen based on a higher spatial resolution instead of height resolution. The DEM's were GIMP DEM and TANDEM-X DEM [Rizollie et al., 2017]. After reprocessing multiple times, the visual quality of the processing chain including the GIMP DEM was higher. TANDEM-X-DEM has a spatial resolution of 90m and a vertical Root Mean Squared Error (RMSE) of 8-12m while the GIMP DEM has a spatial resolution of 30m and a RMSE 8-12m. Interferograms resulting from the TANDEM-X DEM were noisier than interferograms resulting from the GIMP DEM. The horizontal resolution of the DEM proved to be more important due to higher spatial height variability in the AOI, than the vertical resolution. The SAR data used in this case study contains multiple errors that must be corrected for as shown in the methods section. Atmospheric disturbances in the image may not have been fully corrected for and may introduce noise, especially in 2018. The 2018 year was colder than normal and was one of the years with the most snow precipitation in the weather reporting record of Greenland [NSIDC, 2016-2018]. Heavy snowfall, late start of the melt-season and visible ground ice are all possible explanations for extra noise in the early interferograms of May and June 2018. Using the linear atmospheric correction from TRAIN the standard deviation for the displacement velocity decreased. The power law correction [Bekeart et al., 2015] increased the standard deviation and created artificial patterns and was therefore not implemented. The image acquisitions for this case study have been collected between the beginning of June until the end of September based on a mean thawing season for the east coast of Greenland. If the thawing season in the respective years last longer or start earlier, the results do not show the complete seasonal deformation. The vertical displacements are calculated from the LOS displacement assuming only vertical displacement which may introduce small bias. The PS-algorithm of StaMPS performed well in this lowly vegetated natural area with partial spatial and temporal correlation in deformation compared to other PS-processors, that require highly coherent surfaces and deformation patterns.

4.2 Effect of tundra fire on subsurface displacements

Previous research found that tundra fires change seasonal subsidence, and this can be inferred from InSAR analysis [Iwahana et al., 2016 and Liu et al., 2014]. The tundra fire impact is measured using the DNBR fire severity [Allen and Sorbel, 2008] which, shows a minor but statistically significant relation with the seasonal displacement velocity of -2.02 mm/yr. The differences between 2016 and 2018 for both burned and unburned area show a normalized negative difference in relative displacement of approximately 4mm, which is smaller than the cm subsidence after fire impact reported by Liu et al., 2014. Possible reasons why the fire impact on subsidence may have been comparably small after the Greenland fire include thin organic soils and the climatic differences between 2016 and 2018. Firstly, the permafrost in the AOI is continuous but has only a thin overburden (unconsolidated layer < 5m [Zhang et al., 2008]) on top of the bedrock, the possible thickening of the active layer and top down thawing of the permafrost is therefore minimal in comparison with the thicker organic soils in the area of the Anaktuvuk river fire in Alaska [Brown et al., 2002]. Secondly, 2016 and 2018 were both extremes for both warm and cold years. Comparing between those two years of data may be constrained. The thawing season in 2016 started early and the summer was warm resulting in a high seasonal melt and consequent subsidence [National Snow and Ice Data Center (NSIDC) -2016]. Snow melt in 2018 started late after record-breaking snowfall in the late winter. Snow covered the AOI until end of June, adding noise to early interferograms and shortening the thawing season [Pepe and Caló 2017]. Because no ground truth was available, the data of both years can only be compared using the unburned area as control area. From previous research [Iwahana et al., 2016 and Liu et al., 2014] I expected both the mean displacement velocity of 2018 and the velocity difference between 2016 and 2018 to be correlated with the fire severity. Only the displacement velocity of 2018 showed a significant relation to the DNBR fire severity. The relation is minor and still holds major uncertainties and should therefore be treated with care, even though the trend is statistically significant.

4.3 Relation of displacement with greenness and topography

I also examined the influence of pre-fire vegetation greenness in relation to displacement. The NDVI is a measure vegetation health and cover. Indirectly this may be a measure for the thickness of the peat layer which is related to the fuel availability. The thickness of the organic soil determines the maximum subsidence for that area. The NDVI showed a statistically significant positive relation with the post-fire DNBR. This relation directly links fuel to tundra fire severity which has a clear correlation [Jones et al., 2009]. The bar and scatter plot (Figure 3.2.2.1 and Figure 3.2.2.2) with NDVI and displacement did not demonstrate dependency of subsidence on vegetation greenness. The height of an area can be translated to a measure of rockiness in our AOI. Since rocky areas should have less possible subsidence due to a thin topsoil, we expect a correlation between the relative displacement and the height of an area. This correlation is 0.005 mm/y per m height difference. The difference between the minimum and maximum height in the area is approximately 650m resulting in a maximal difference of 3.25 mm/year which is a statistically insignificant trend. The aspect shows a minor difference of maximum 2mm/year on north and east facing hills which, is also insignificant with the multiple centimetres of relative displacements in this area. The sun projecting difference between north and south facing hills is insignificant at high latitudes, the main driver is therefore wind direction. The wind in the AOI is mostly from the north or east causing rain and snow to possibly have more disturbance on north and east facing hills.

4.4 Recommendations for future research

Even though the PS-InSAR results look promising for monitoring subsidence, there may be several improvements. Firstly, results may improve using combined SBAS and PS processing. Processing both SBAS and PS creates 2 data sets with a unique coverage which can be combined to retrieve higher accuracy and more measurement points [Shanker et al., 2011]. A second possible improvement is the integration of L-band SAR acquisitions from Advanced Land Observing Satellite-2 (ALOS-2) by the Japan Aerospace Exploration Agency (JAXA), with a revisit time of 14 days, in the analysis.

ALOS-2 data can be pre-processed using SNAP but could be handled by other pre-processing software as well, the interferograms will be handled by StaMPS in the same manner. L-band SAR offers lower decorrelation over vegetated areas [Wei and Sandwell, 2010] while C-band offers higher deformation accuracy [Sandwell et al., 2008], using both these advantages may improve the accuracy of the displacement results [Xiaobing et al., 2009]. The difference in incidence angle and acquisition date diversifies the data and may improve accuracy. The extra data set may also act as a validation data set making the displacement measurements more absolute. This additional data cannot solve the incompatibility between the two years of data. To improve on interannual compatibility better atmospheric correction and data selection based on weather data is key. In this research only phase computed atmospheric correction is used but TRAIN also offers atmospheric correction based on weather model (European Centre for Medium-Range Weather Forecasts) ECMWF Re-Analysis (ERA) and satellite Moderate Resolution Imaging Spectroradiometer (MODIS) which can be used to correct the results for 2016 and 2018[Bekeart et al., 2015]. Together with data from the Danish Meteorological Institute (DMI), or other local weather and climatic data centres, the SAR acquisitions can be selected on snow cover, place in thaw season and atmospheric conditions. The last recommendation is specifically to improve the potential of InSAR computed displacements for large scale climate research and fire forced feedback loops. Combining ground measurements of seasonal subsidence, porosity, permafrost content, water content and carbon content; the water-to-ice subsidence model by Liu et al., (2012) and InSAR computed displacements it may be possible to spatially extrapolate carbon emissions from permafrost degradation due to tundra fires over larger areas.

5. CONCLUSIONS

PS-InSAR showed great possibilities for computing seasonal deformation, over continuous permafrost with low vegetation cover, with the improved revisit time of C-band SAR satellites Sentinel-1A and 1B. The seasonal subsidence did not change drastically from the pre-fire to the post-fire year as had been expected from previous research. The relation between post-fire displacement and fire severity showed a minor statistically significant trend of -2.02 mm/yr. The pre-fire vegetation greenness, and topography showed no statistically significant relation with the displacement. The lack of drastic change over the burned area could be explained by the thin organic soils in these tundra ecosystems of western Greenland. Some of the differences between our analysis year 2016, the year before the fire, and 2018, the year after the fire, may be masked by large climatic differences between those two years. Inclusion of more years and normalizing for interannual weather variability could further improve the interpretation of the results. Further improvement could come from combined SBAS-PS processing, inclusion of L-band SAR data, inclusion of ground measurements and improved atmospheric correction. In summary, the InSAR-derived seasonal displacements are a useful proxy of active layer change over the growing season, yet the fire impact on seasonal displacement was smaller than experiment. Further analyses on fire-induced vertical displacements should therefore examine the relationship with organic layer thickness, to further quantify the impacts of tundra fires on permafrost degradation

6. ACKNOWLEDGEMENTS

I thank Dr. Sander Veraverbeke and Dr. Kanayim Teshebaeva for their expertise and consultancy on this project. I also thank Dr. Jose Manuel Delgado Blasco and other contributors to the STEP forum for their direct help with software issues and software development. This project is part of the course AB_1096 of the Bachelor of Science program for Earth Sciences of the Earth and climate department from the faculty of BETA sciences at free university Amsterdam.

7. REFERENCES

- Allen, J. and Sorbel, B. (2008) Assessing the differenced Normalized Burn Ratio's ability to map burn severity in the boreal forest and tundra ecosystems of Alaska's national parks. International Journal of Wildland Fire, 17: 463–475. DOI: <https://doi.org/10.1657/1938-4246-45.1.64>
- Bekaert, D.P.S.; Walters, R.J.; Wright, T.J.; Hooper, A.J.; Parker, D.J. (2015) Statistical comparison of InSAR tropospheric correction techniques. Remote Sens. Environ. 2015, 170, 40–47. DOI: <https://doi.org/10.1016/j.rse.2015.08.035>
- Bowman, David M. J. S., Balch, Jennifer K., Artaxo, Paulo, Bond, William J., Carlson, Jean M., Cochrane ,Mark A., D'Antonio , Carla M., DeFries, Ruth S. , Doyle, John C., Harrison, Sandy P., Johnston, Fay H. , Keeley, Jon E., Krawchuk, Meg A., Kull, Christian A., Marston, J. Brad., Moritz, Max A., Prentice, I. Colin, Roos, Christopher I., Scott, Andrew C., Swetnam, Thomas W., van der Werf, Guido R., Pyne, Stephen J., (2009) **Fire in the Earth System**, May 2009 Science 324(5926):481-4. DOI: 10.1126/science.1163886
- Brown, J., O. Ferrians, J. A. Heginbottom, and E. Melnikov. (2002) **Circum-Arctic Map of Permafrost and Ground-Ice Conditions, Version 2**. Boulder, Colorado USA. NSIDC: National Snow and Ice Data Center. DOI: [date accessed 10th May 2019].
- CAVM Team. (2003). **Circumpolar Arctic Vegetation Map (1:7,500,000 scale), Conservation of Arctic Flora and Fauna (CAFF) Map No. 1**. U.S. Fish and Wildlife Service, Anchorage, Alaska. ISBN: 0-9767525-0-6, ISBN-13: 978-0-9767525-0-9
- Chen, C. W. and H. A. Zebker, (2001) Two-dimensional phase unwrapping with use of statistical models for cost functions in nonlinear optimization, Journal of the Optical Society of America A, vol. 18, pp. 338-351 DOI: <https://doi.org/10.1364/JOSAA.18.000338>
- Copernicus, **Sentinel data 2016 and 2018**. Retrieved from [ASF DAAC](#) April 2019, processed by ESA.
- Crosettoa, Michele, Oriol Monserrata, María Cuevas-González, Núria Devanthérya, Bruno Crippaba, (2016) **Persistent Scatterer Interferometry: A review** DOI: <https://doi.org/10.1016/j.isprsjprs.2015.10.011> - ISPRS Journal of Photogrammetry and Remote Sensing Volume 115, May 2016, Pages 78-89
- Deea, D. P., S. M. Uppalaa, A. J. Simmonsa, P.Berrisforda, P.Polia, S. Kobayashib,U. Andraec,M.A.Balmasedaa,G.Balsamoa,P.Bauera,P.Bechtolda,A.C.M.Beljaarsa,L. van de Bergd,J.Bidlota,N.Bormanna,C.Delsola,R.Dragania,M.Fuentesa,A.J.Geera,L. Haimbergere,S.B.Healya,H.Hersbacha,E.V.H olma,L.Isaksena,P.K allbergc,M. K öhlera, M. Matricardia,A.P.McNallya,B.M.Monge-Sanzf, J.-J. Morcrettea,B.-K.Parkg,C. Peubeya,P.deRosnaya,C.Tavolatoe, J.-N. Th épautaand F. Vitarta (April 2011) **The ERA-Interim reanalysis: configuration and performance of the data assimilation system** Quarterly Journal of the Royal Meteorological Society Q. J. R. Meteorol. Soc. 137: 553 – 597, DOI: <https://doi.org/10.1002/qj.828>
- Dmitry A Streletskiy O. A. Anisimov and Vasiliev Alexander, (2015) **Permafrost degradation** DOI: 10.1016/B978-0-12-394849-6.00010-X
DOI 10.1126/science.1163886, Science : Vol. 324, Issue 5926, pp. 481-484
- F. Foroughniaa, S. Nematia, Y. Maghsoudia,*, D. Perissinb, (2019) **An iterative PS-InSAR method for the analysis of large spatio-temporal baseline data stacks for land subsidence estimation**, DOI: <https://doi.org/10.1016/j.jag.2018.09.018> , in International Journal of Applied Earth Observation and Geoinformation Volume 74, February 2019, Pages 248-258
- Ferretti, Alessandro, Claudio Prati, and Fabio Rocca (2001) **Permanent Scatterers in SAR Interferometry**, DOI: 10.1109/36.898661 8th IEEE TRANSACTIONS ON GEOSCIENCE AND REMOTE SENSING, VOL. 39, NO:1
- Foumelis, M., J. M. Delgado Blasco, Y-L. Desnos, M. Engdahl, D. Fernandez, L. Veci, J. Lu and C. Wong. (2018) "ESA SNAP - StaMPS Integrated processing for Sentinel-1 Persistent Scatterer Interferometry". IEEE International Geoscience and Remote Sensing Symposium. IGARSS 2018. DOI:10.5281/zenodo.1322353

- Garcia, L. J. M. and Caselles, V. (**1991**) **Mapping burns and natural reforestation using Thematic Mapper data**, DOI: 10.1080/10106049109354290 , Geocarto International 6(1):31-37
- Geophysical research letters 31 (23)
- Gibson, C., Chasmer, L., Thompson, D., Quinton, W., Flannigan, M. and Olefeldt, D. (**2018**). **Wildfire as a major driver of recent permafrost thaw in boreal peatlands**. DOI: 10.1038/s41467-018-05457-1, *Nature Communications*, 9(1).
- Goldstein, Richard M. and Charles L. Werner (**1998**) **Radar interferogram filtering for geophysical applications**. *Geophysical Research Letters*, 25, 4035-4038 November 1998 DOI: 10.1029/1998GL900033
- Grzesiak, Karolina and Wojciech J. Milczarek (**2003**) **LOS Displacements of Mauna Loa volcano, Hawaii Island, as determined using SBAS-InSAR**, DOI: 10.1051/e3sconf/20175500006
- Gunce, H.B.; San, B.T. (**2017**) **Measuring Earthquake-Induced Deformation in the South of Halabjah (Sarpol-e-Zahab) Using Sentinel-1 Data** on November 12, 2017. *Proceedings* 2018,2, 346. DOI: 10.3390/ecrs-2-05159
- Hansen, James and Nazarenko, Larissa (**jan-13-2004**) **Soot climate forcing via snow and ice albedos** DOI: doi.org/10.1073/pnas.2237157100, in PNAS,
- Hinzman, L., D. Kane, R. Gieck, and K. Everett (**1991**), **Hydrologic and thermal properties of the active layer in the Alaskan Arctic**, DOI: 10.1016/0165-232X(91)90001-W, *Cold Reg. Sci. Technol.*, 19(2), 95–110.,
- Hooper A; Bekaert D; Spaans K; Arikan M (**2012**), **Recent advances in SAR interferometrytime series analysis for measuring crustal deformation**, *Tectonophysics*, 514-517, pp.1-13. DOI: 10.1016/j.tecto.2011.10.013
- Hooper, A, H Zebker, P Segall, B Kampes, (**2004**) **A new method for measuring deformation on volcanoes and other natural terrains using InSAR persistent scatterers** DOI: https://doi.org/10.1029/2004GL021737
- Hooper, A., (**2008**) **A multi-temporal InSAR method incorporating both persistent scatterer and small base-line approaches**, *Geophys. Res. Lett.*, 35, L16,302, DOI: 10.1029/2008GL03465.
- Hooper, A., and H. Zebker, (**2007**) **Phase unwrapping in three dimensions with application to InSAR timeseries** DOI: https://doi.org/10.1364/JOSAA.24.002737 *J. Opt. Soc. Amer. A*, 24, 2737–2747, 2007
- Hooper, A., P. Segall, and H. Zebker, (**2007**) **Persistent scatterer InSAR for crustal deformation analy-sis, with application to Volcano Alcedo, Galapagos**, *J. Geophys. Res.*, 112(B07407), DOI:10.1029/2006JB004763, 2007
- Hooper, A.J.; Bekaert, D.; Hussain, E.; Spaans, K. (**2017**) **StaMPS/MTI Manual**; School of Earth and Environment: Leeds, UK, 2018
- Howat, I., A. Negrete, and B. Smith. (**2014**). **The Greenland Ice Mapping Project (GIMP) land classification and surface elevation data sets**, *The Cryosphere*. 8. 1509-1518. DOI:<https://doi.org/10.5194/tc-8-1509-2014>
- Howat, I., A. Negrete, and B. Smith. (**2015**). **MEASUREs Greenland Ice Mapping Project (GIMP) Digital Elevation Model, Version 1**. [1.1.2v2]. Boulder, Colorado USA. NASA National Snow and Ice Data Center Distributed Active Archive Center.
- DOI:<https://doi.org/10.5067/NV34YUIXLP9W>. [Date Accessed = May-10th 2019].
- Ittycheria, Nikitha , Divya Sekhar Vaka, Y. S. Rao (**2018**) **Time series analysis of surface deformation of Bengaluru city using Sentinel-1 images**, DOI: 10.5194/isprs-annals-IV-5-473-2018
- Iwahana, Go, Uchida, Masao, Liu, Lin, Gong, Wenyu, Meyer, Frnaz J., Guritz, Richard, Yamanokuchi, Tsutomu and Hinzman, Larry (**march-8-2016**) **InSAR detection and field evidence for Thermokarst afrer a tundra wildfire, using ALOSPALSAR**, DOI:10.3390/rs8030218 in *Remote sensing*
- Jones, Benjamin M., Kolden, Crystal A., Jandt, Randi, Abatzoglou, John T., Urban, Frank, Arp, Christopher D. (**2009**) **Fire Behavior, Weather, and Burn Severity of the 2007 Anaktuvuk**

River Tundra Fire, North Slope, Alaska. DOI:10.1657/1938-4246-41.3.309 2009/08/01 Arctic, Antarctic, and Alpine Research

Key, Carl H. and Nate Benson, (1999) **measuring and remote sensing of burn severity: the CBI and NBR - Proceedings Joint Fire Science Conference and Workshop** Volume: II

Lawrence DM, Slater AG, Tomas RA, Holland MM, Deser C. (2008) **Accelerated Arctic land warming and permafrost degradation during rapid sea ice loss.** Geophysical Research Letters. 2008;35:L11506. DOI: doi: 10.1029/2008GL033985

Leeuwen, van Gijs, (accessed June-july 2019) <https://github.com/gjvanleeuwen/SNAP-StaMPS-Visualizing>

Liu, L., E. E. Jafarov, K. M. Schaefer, B. M. Jones, H. A. Zebker, C. A. Williams, J. Rogan, and T. Zhang (2014), **InSAR detects increase in surface subsidence caused by an Arctic tundra fire,** DOI:10.1002/2014GL060533. Geophys. Res. Lett., 41, 3906– 3913,

Main-Knorn, Magdalena, Bringfried Pflug, Jerome Louis, Vincent Debaecker, Uwe Müller-Wilm, Ferran Gascon , (2017) **Sen2Cor for Sentinel-2** DOI: 10.1111/12.2278218

Mazhitova G. G. (2000) **Pyrogenic dynamics of permafrost-affected soils in the Kolyma upland.** Eurasian Soil Science 33: 542–551.

Min-Jeong Jo, Hyung-Sup Jung & Sung-Ho Chae (2018) **Advances in three-dimensional deformation mapping from satellite radar observations: application to the 2003 Bam earthquake,** Geomatics, Natural Hazards and Risk, 9:1, 678-690, DOI:10.1080/19475705.2018.1473293

National Snow and Ice Data Center (NSIDC) - <https://nsidc.org/> - [date accessed – June/July 2019] – Melt season data for 2016 and 2018.

Pepe, Antonio and Calò, Fabiana, (2017) **A Review of Interferometric Synthetic Aperture RADAR (InSAR) Multi-Track Approaches for the Retrieval of Earth's Surface Displacements,** Appl. Sci. 2017, 7(12), 1264; DOI: <https://doi.org/10.3390/app7121264>

Prats-Iraola, P.; Nannini, M.; Yague-Martinez, N.; Scheiber, R.; Minati, F.; Vecchioli, F.; Costantini, M.; Borgstrom, S.; De Martino, P.; Siniscalchi, V.; et al. (2016) **Sentinel-1 tops interferometric time series results and validation.** In Proceedings of the 2016 IEEE International Geoscience and Remote Sensing Symposium (IGARSS), Beijing, China, 10–15 July 2016; pp. 3894–3897. DOI:10.1109/IGARSS.2016.7730011

Rizzoli, P., Martone, M., Gonzalez, C., Wecklich, C., Borla Tridon, D., Bräutigam, B., Bachmann, M., Schulze, D., Fritz, T., Huber, M., Wessel, B., Krieger, G., Zink, M., and Moreira, A. (2017): **Generation and performance assessment of the global TanDEM-X digital elevation model.** ISPRS Journal of Photogrammetry and Remote Sensing, Vol 132, pp. 119-139. DOI:<https://doi.org/10.1016/j.isprsjprs.2017.08.008>

Rocha, Adrian V. and Shaver, Gaius R. (11-apr-2011), **Postfire energy exchange in Arctic Tundra: The importance and climatic implications of burn severity,** DOI doi.org/10.1111/j.1365-2486.2011.02441.x in Global Change Biology Vol17, Issue 9

Rocha, Adrian V., Lorantz, Michael M., Higuera, Phil E., Mack, Michelle C., Hu, Feng Sheng, Jones, Benjamin M., Breen, Amy L., Rastetter, Edward B., Goetz, Scott J. and Shaver, Gus R., (19-dec-2012), **The footprint of Alaskan tundra fires during the past half-century: implications for surface properties and radiative forcing,** DOI 10.1088/1748-9326, Environmental Research Letters Vol. 7, N. 4

Roush, J.W., R.H. Haas, J.A. Schell, D.W. Deering, (1973) **monitoring vegetation systems in the great plains**

Sandwell, D.T.; Myer, D.; Mellors, R.; Shimada, M.; Brooks, B. Foster, J. (2008) **Accuracy and Resolution of ALOS Interferometry: Vector Deformation Maps of the Father's Day Intrusion at Kilauea.** IEEE Trans. Geosci. Remote Sens. 2008, 46, 3524–3534. DOI: DOI: 10.1109/TGRS.2008.2000634

Schuur, Edward A. G. James Bockheim, Josep G. Canadell, Eugenie Euskirchen, Christopher B. Field, Sergey V. Goryachkin, Stefan Hagemann, Peter Kuhry, Peter M. Lafleur, Hanna Lee, Galina Mazhitova, Frederick E. Nelson, Annette Rinke, Vladimir E. Romanovsky, Nikolay Shiklomanov,

Charles Tarnocai, Sergey Venevsky, Jason G. Vogel, Sergei A. Zimov, (2008) **Vulnerability of Permafrost Carbon to Climate Change: Implications for the Global Carbon Cycle**, *BioScience*, Volume 58, Issue 8, September 2008, Pages 701–714, DOI:<https://doi.org/10.1641/B580807>

Shanker, Piyush, Francesco Casu, Howard A. Zebker, and Riccardo Lanari, (2011) **Comparison of Persistent Scatterers and Small Baseline Time-Series InSAR Results: A Case Study of the San Francisco Bay Area** 592IEEE GEOSCIENCE AND REMOTE SENSING LETTERS, VOL. 8, NO. 4, JULY 2011 DOI: 10.1109/LGRS.2010.2095829

Sousa, Joaquim Andy Hooper Ramon F Antonio, Miguel Ruiz-Armenteros (2011) **Persistent Scatterer InSAR: A comparison of methodologies based on a model of temporal deformation vs. spatial correlation selection criteria**, October 2011 *Remote Sensing of Environment* 115(10):2652-2663 DOI: 10.1016/j.rse.2011.05.021 Project: Plataforma de Inovação da Vinha e do Vinho (PVV)

Tomás Roberto, Roberto TomásG. HerreraG. HerreraJuan Manuel Lopez-SánchezJuan Manuel Lopez-Sánchez Jordi J. MallorquiJordi J. Mallorqui, (2010) **Study of the land subsidence in Orihuela City (SE Spain) using PSI data: Distribution, evolution and correlation with conditioning and triggering factors** September 2010 *Engineering Geology* 115(1):105-121 DOI: 10.1016/j.enggeo.2010.06.004

Veci, L.; Lu, J.; Prats-Iraola, P.; Scheiber, R.; Collard, F.; Fomferra, N.; Engdahl, M. (2014) **The Sentinel-1 Toolbox.** In Proceedings of the IEEE International Geoscience and Remote Sensing Symposium (IGARSS), Quebec City, QC, Canada, 13–18 July 2014; pp. 1–3

Wei, M.; Sandwell, D.T. (2010) **Decorrelation of L-Band and C-Band Interferometry over Vegetated Areas in California.** *IEEE Trans. Geosci. Remote Sens.* 2010, 48, 2942–2952. DOI:10.1109/TGRS.2010.2043442

Zan, De, F.; Guarnieri, A.M. (2006) **TOPSAR: Terrain observation by progressive scans.** DOI: *IEEE Trans. Geosci. Remote Sens.* 2006, 44, 2352–2360. DOI:10.1109/TGRS.2006.873853

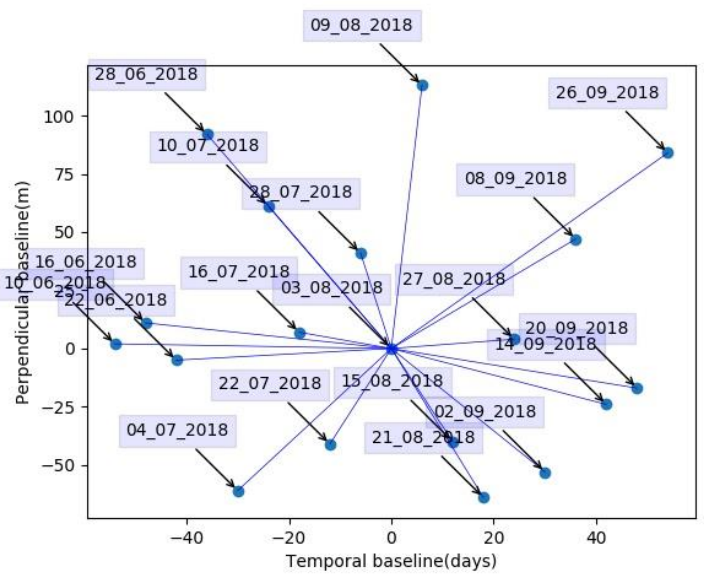
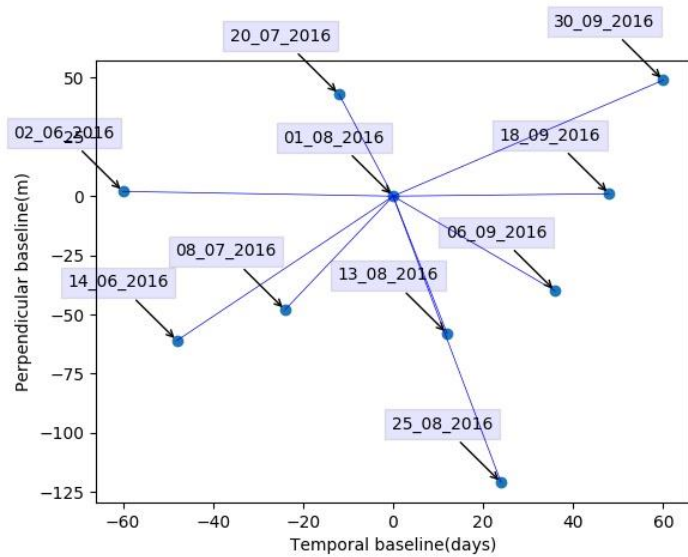
Zhang, Tingjun, Roger Graham Barry, K. Knowles, J. A. Heginbottom, Jervon Brown (2008) **Bryant & Stratton CollegeStatistics and characteristics of permafrost and ground-ice distribution in the Northern Hemisphere**, DOI: 10.1080/10889370802175895 March 2008 *Polar Geography* 31(1):47-68

Zhu, Z. C.H. , Key, D., Ohlen., N. Benson, (2006) **Evaluate Sensitivities of Burn-Severity Mapping Algorithms for Different Ecosystems and Fire Histories in the United States.**

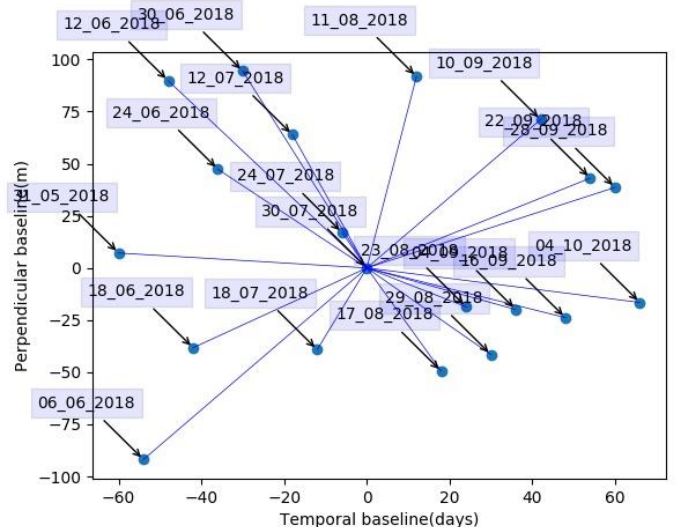
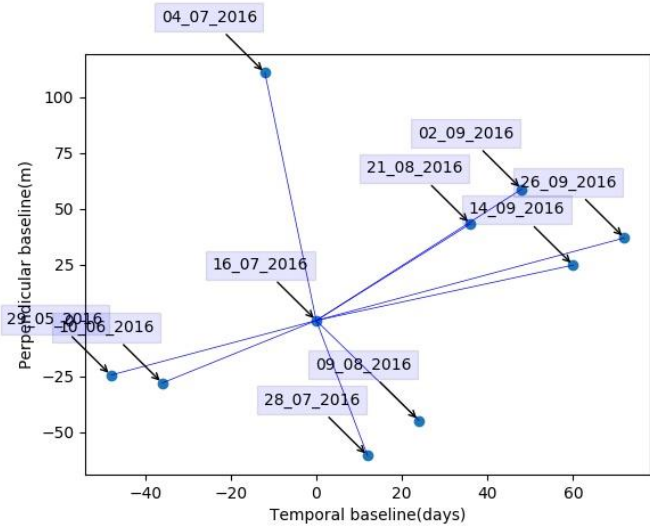
Zhou, Xiaobing, N.Chang and S. Li, (2009) **Applications of SAR Interferometry in Earth and Environmental Science Research.** *Sensors* 2009, 9, 1876-1912; DOI:10.3390/s90301876

Zoltai S. C. (1993) **Cyclic development of permafrost in the peatlands of northwestern Alberta, Canada.** *Arctic and Alpine Research* 25 : 240–246.

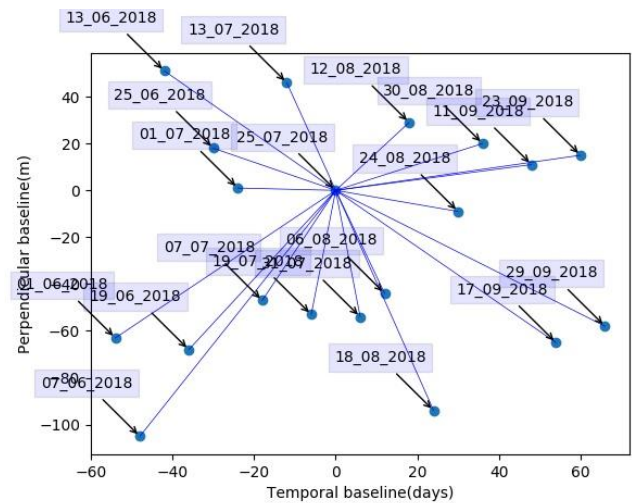
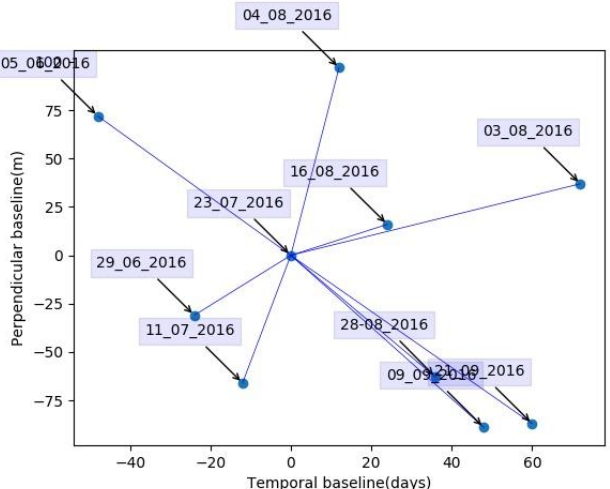
8. APPENDICES



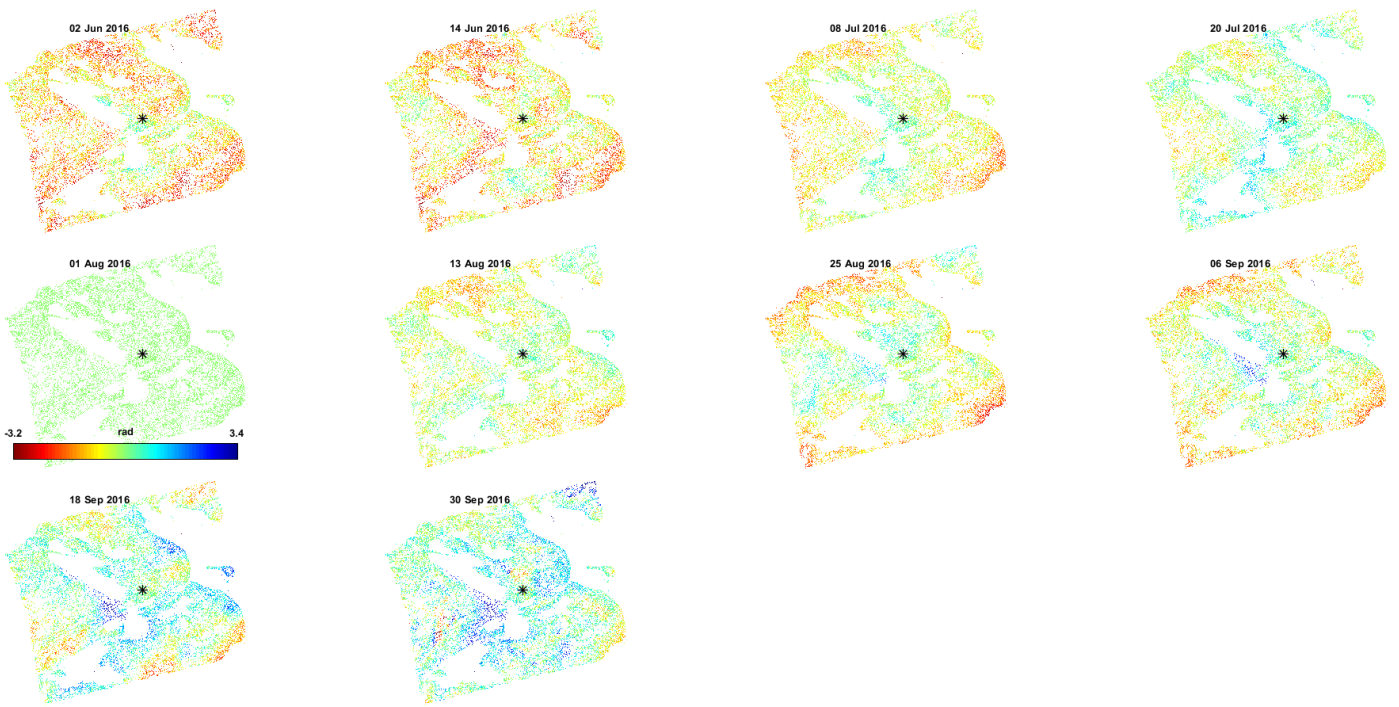
Appendice 1: Baseline plots for ascending track 90/222 for both 2016 and 2018



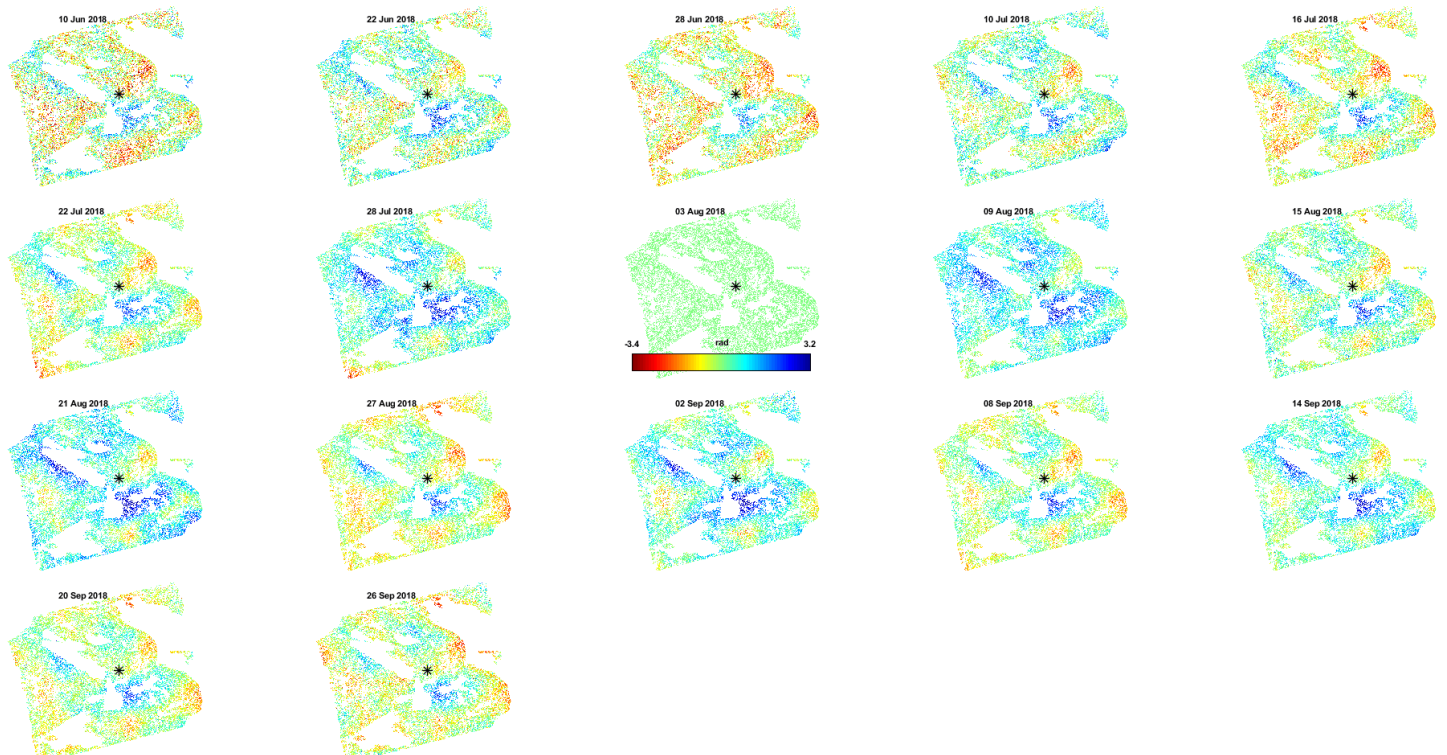
Appendice 2: Baseline plots for descending track 25/365 for both 2016 and 2018



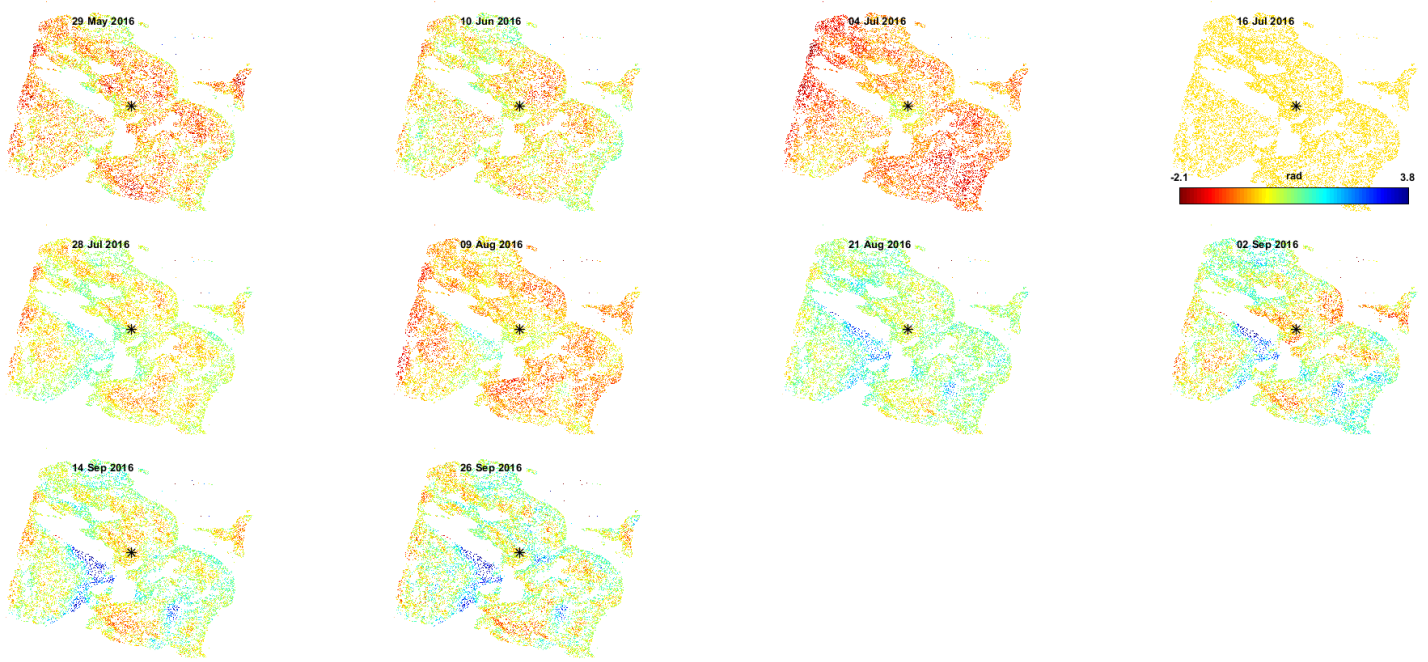
Appendice 3: Baseline plots for descending track 127/366 for both 2016 and 2018



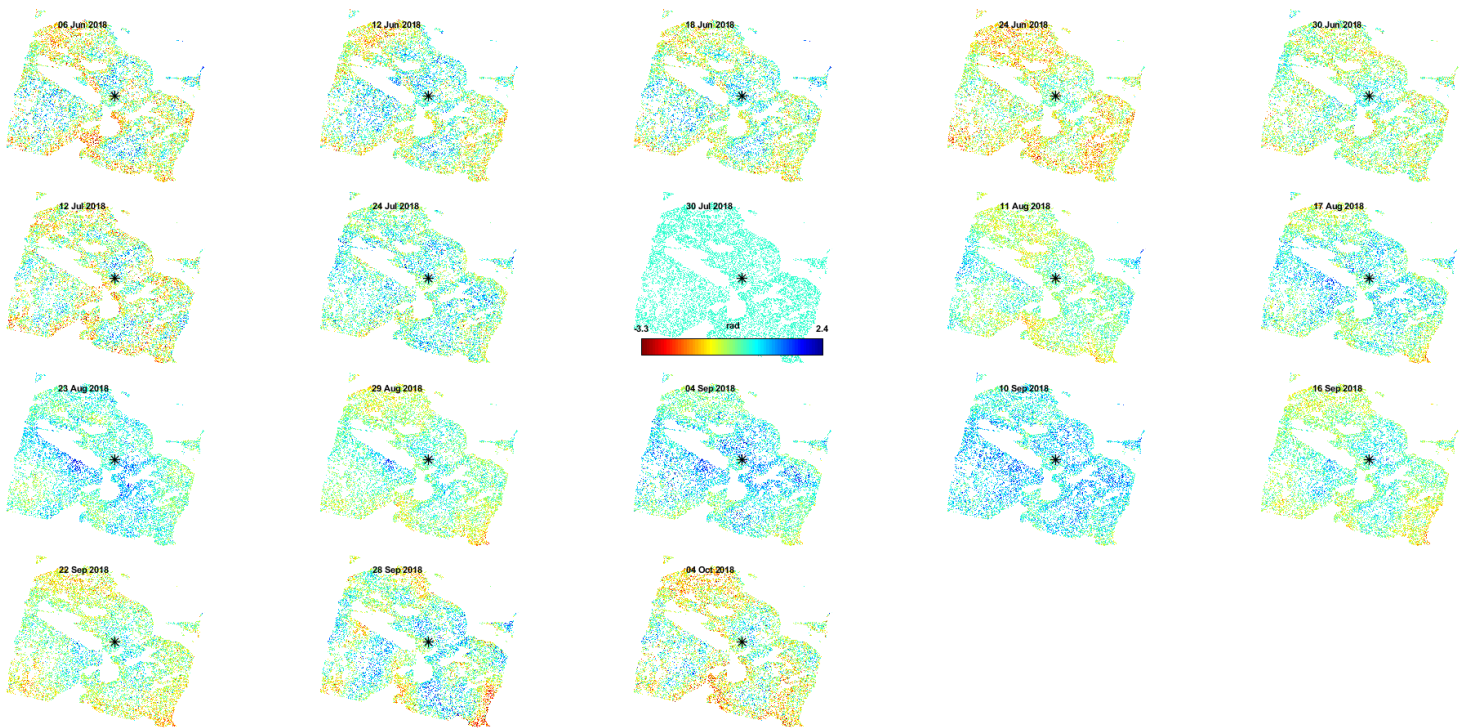
Appendice 4: Unwrapped phase for ascending track 90/~222 year 2016, all displacements are in radians relative to the master and the satellite.



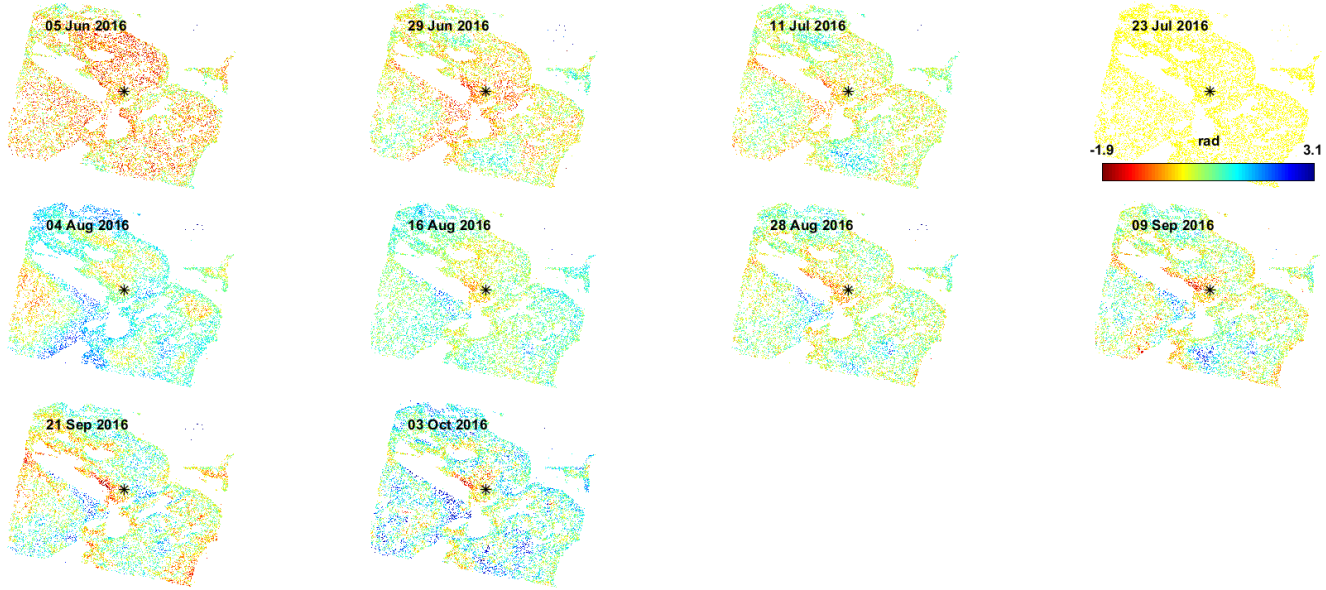
Appendice 5: Unwrapped phase for ascending track 90/~222 year 2018, all displacements are in radians relative to the master and the satellite.



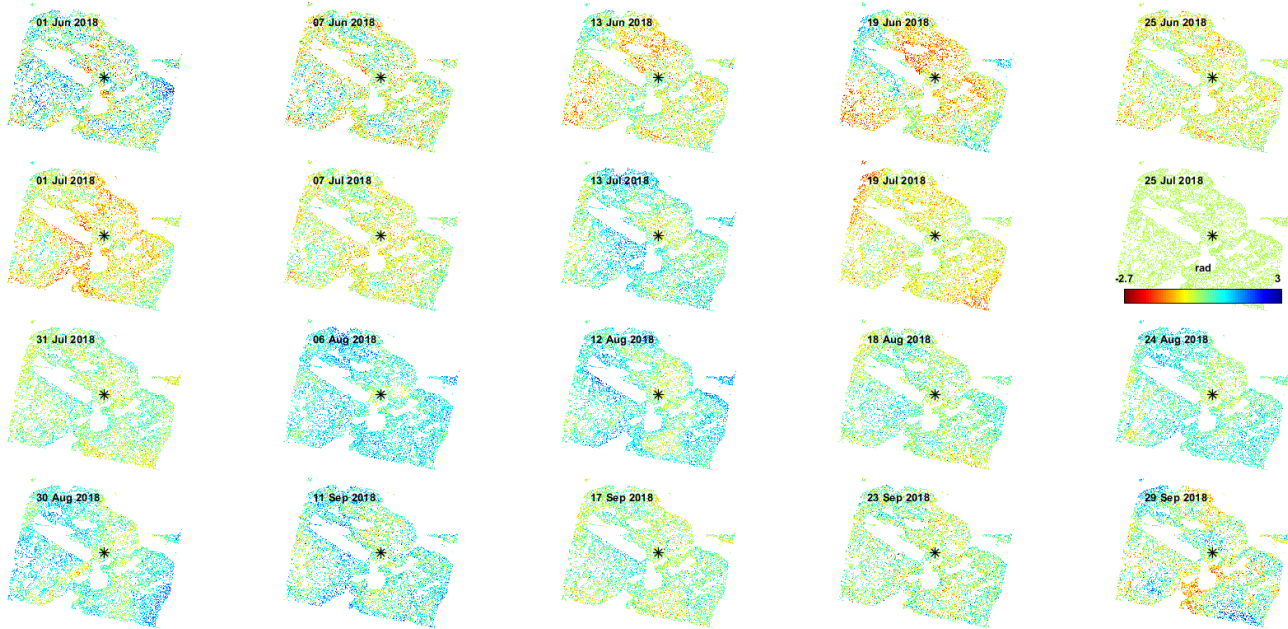
Appendice 6: Unwrapped phase for ascending track 25/~365 year 2016, all displacements are in radians relative to the master and the satellite.



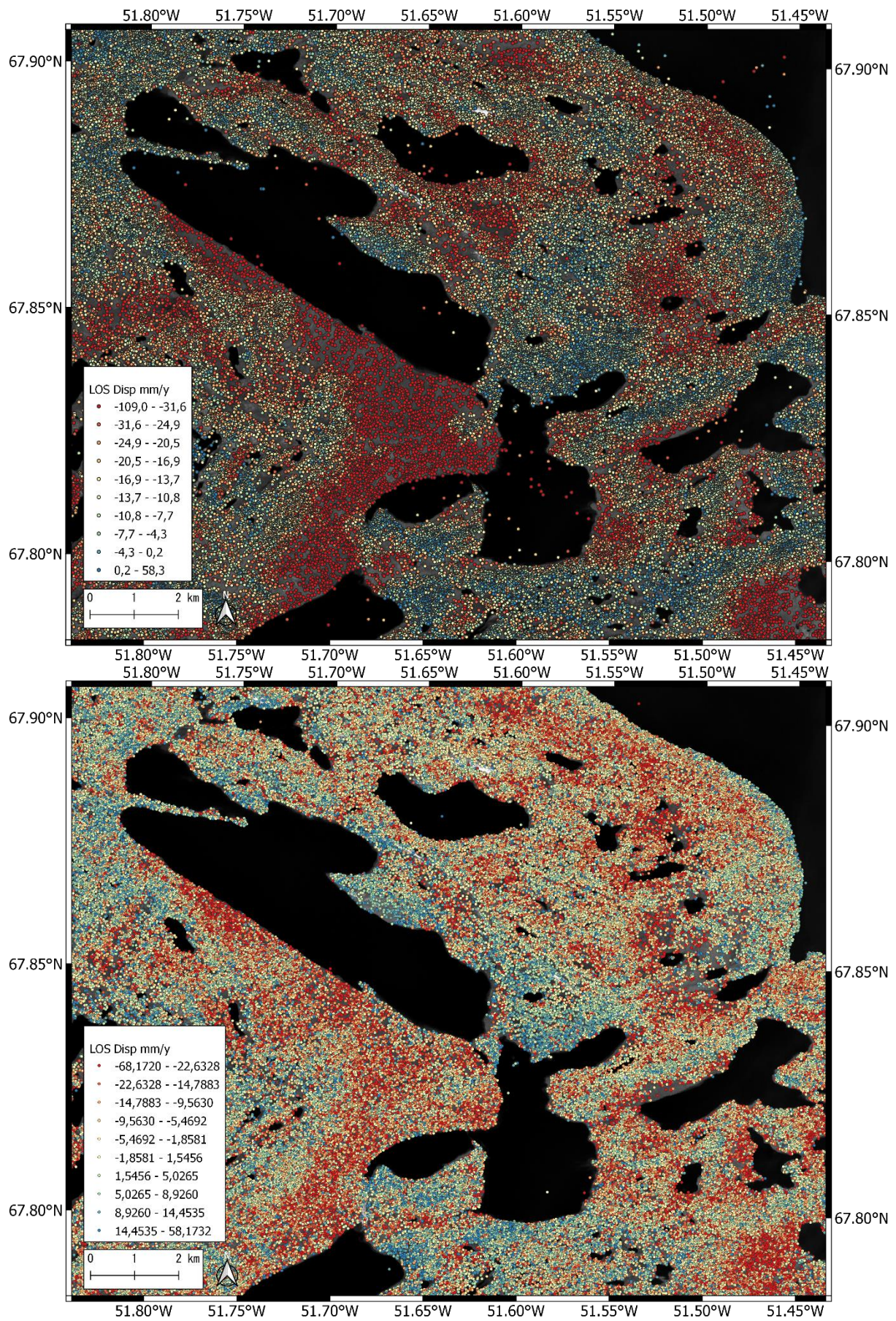
Appendice 7: Unwrapped phase for ascending track 25/~365 year 2018, all displacements are in radians relative to the master and the satellite.



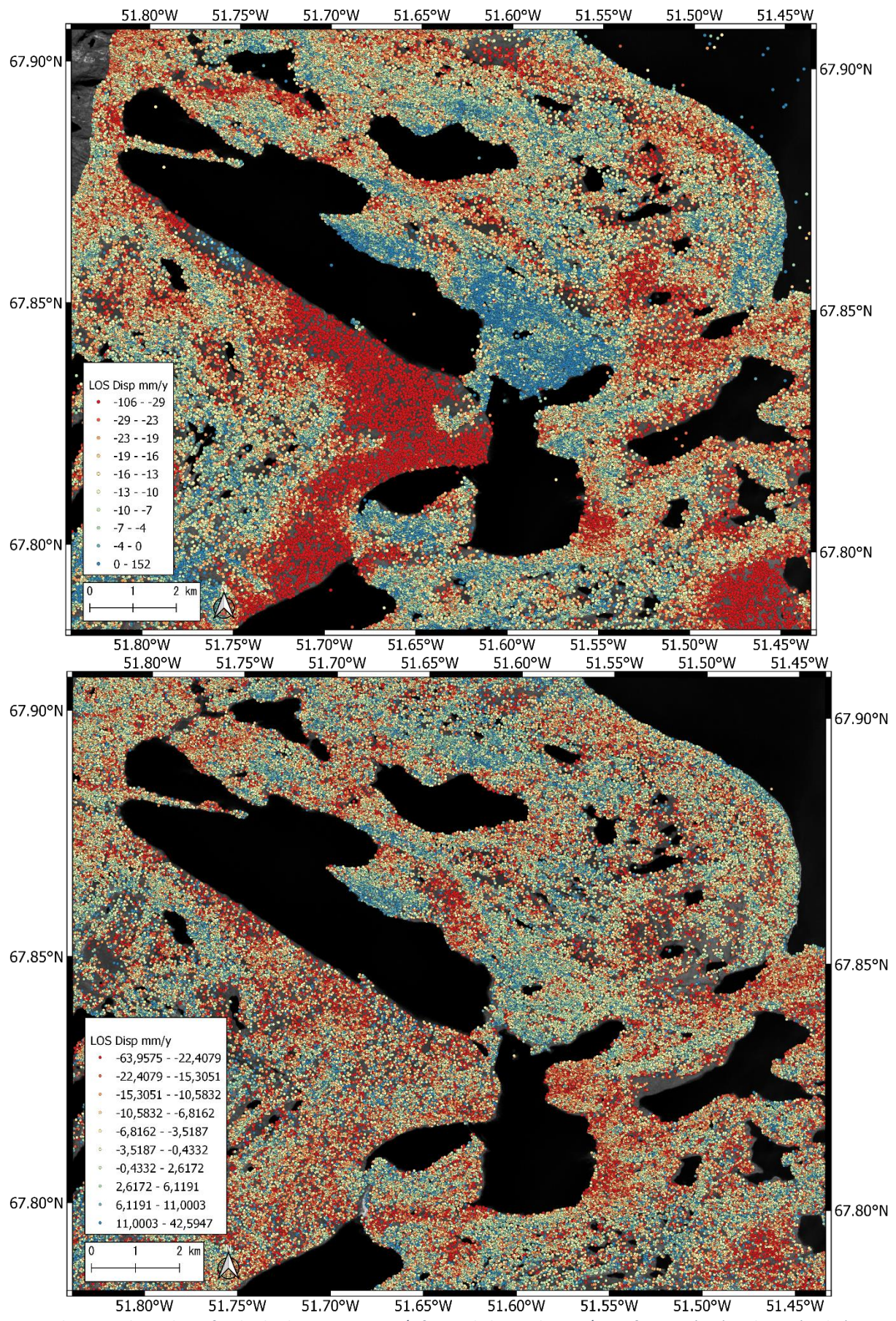
Appendice 8: Unwrapped phase for ascending track 127/~366 year 2016, all displacements are in radians relative to the master and the satellite.



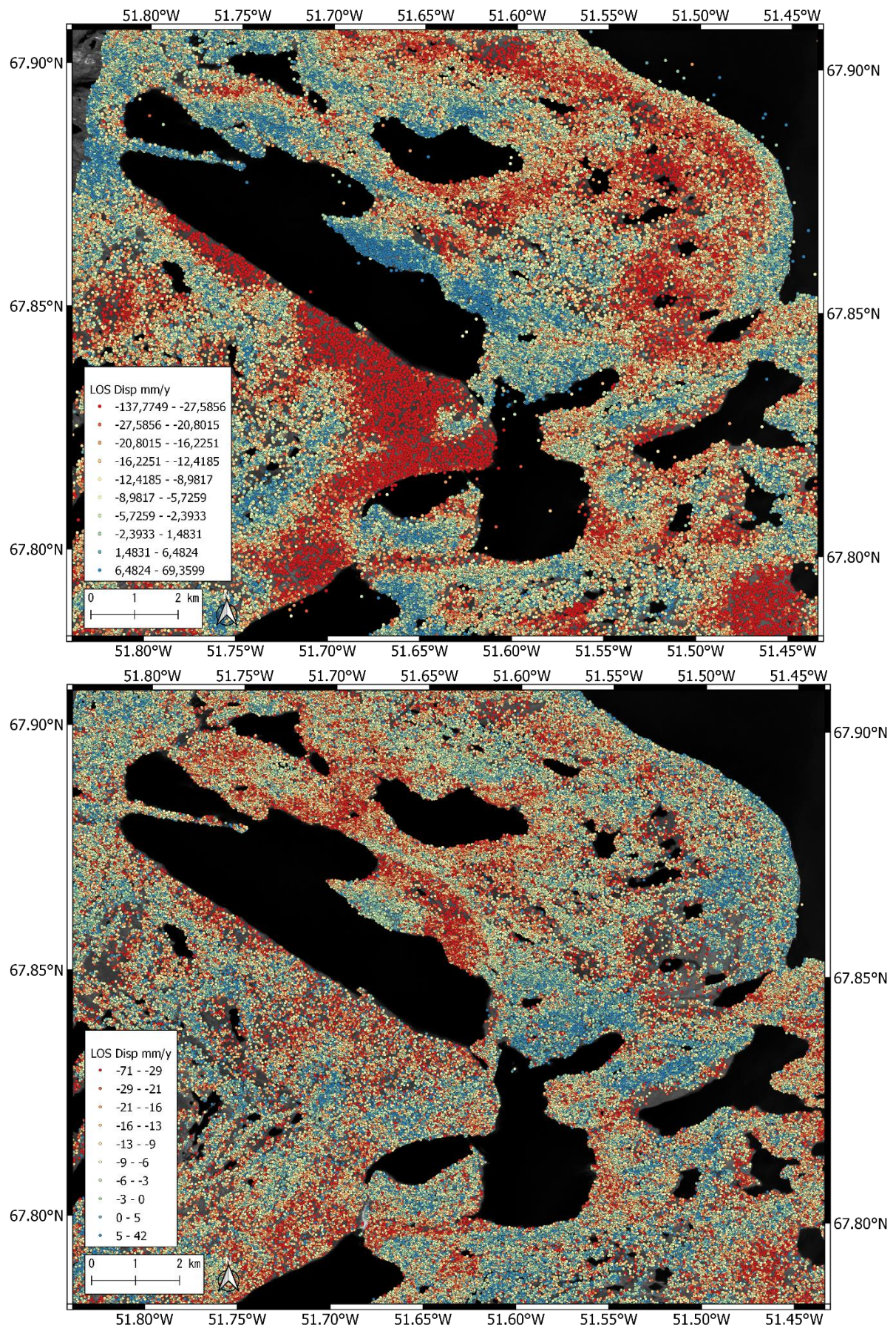
Appendice 9: Unwrapped phase for ascending track 25/~365 year 2016, all displacements are in radians relative to the master and the satellite.



Appendice 10 Relative line of sight displacement in mm/y for track ascending 90/~222 for 2016(top) and 2018(under).



Appendix 11 Relative line of sight displacement in mm/y for track descending 25/~365 for 2016(top) and 2018(under).



Appendice 12 Relative line of sight displacement in mm/y for track descending 127/~366 for 2016(top) and 2018(under).